

---


Electronic Theses and Dissertations, 2004-2019

---

2005

## Design Of A Dynamic Focusing Microscope Objective For Oct Imaging

Supraja Murali  
*University of Central Florida*

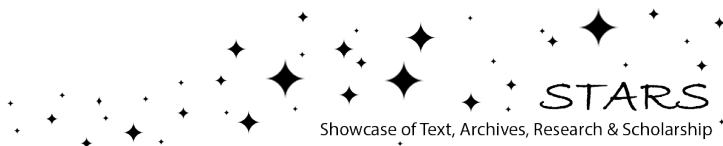
 Part of the [Electromagnetics and Photonics Commons](#), and the [Optics Commons](#)  
Find similar works at: <https://stars.library.ucf.edu/etd>  
University of Central Florida Libraries <http://library.ucf.edu>

This Masters Thesis (Open Access) is brought to you for free and open access by STARS. It has been accepted for inclusion in Electronic Theses and Dissertations, 2004-2019 by an authorized administrator of STARS. For more information, please contact [STARS@ucf.edu](mailto:STARS@ucf.edu).

---

### STARS Citation

Murali, Supraja, "Design Of A Dynamic Focusing Microscope Objective For Oct Imaging" (2005). *Electronic Theses and Dissertations, 2004-2019*. 599.  
<https://stars.library.ucf.edu/etd/599>



# **DESIGN OF A DYNAMIC FOCUSING MICROSCOPE OBJECTIVE FOR OCT IMAGING**

by

**SUPRAJA MURALI**

B.S. Birla Institute of Technology and Science, Pilani, India, 2003

A thesis submitted in partial fulfillment of the requirements  
for the degree of Master of Science  
in the College of Optics and Photonics  
at the University of Central Florida  
Orlando, Florida

Fall Term  
2005

© 2005 Supraja Murali

## ABSTRACT

Optical Coherence Tomography (OCT) is a novel optical imaging technique that has assumed significant importance in bio-medical imaging in the last two decades because it is non-invasive and provides accurate, high resolution images of three dimensional cross-sections of body tissue, exceeding the capabilities of the current predominant imaging technique –ultrasound. In this thesis, high resolution OCT is investigated for *in vivo* detection of abnormal skin pathology for the early diagnosis of cancer. The technology presented is based on a dynamic focusing microscopic imaging probe conceived for skin imaging and the detection of abnormalities in the epithelium. A novel method for dynamic focusing in the biological sample using liquid crystal (LC) lens technology to obtain three dimensional images with invariant resolution throughout the cross-section and depth of the sample is presented and discussed. Two different skin probe configurations that incorporate dynamic focusing with LC lenses, one involving a reflective microscope objective sub-system, and the other involving an all-refractive immersion microscope objective sub-system are investigated. In order to ensure high resolution imaging, a low coherence broadband source, namely a femtosecond mode-locked Ti: sapphire laser centered at a wavelength of approximately 800nm is used to illuminate the sample. An in-depth description and analysis of the optical design and predicted performance of the two microscope objectives designed for dynamic three dimensional imaging at 5 $\mu$ m resolution for the chosen broadband spectrum is presented.

## ACKNOWLEDGEMENTS

I wish to express my gratitude to my graduate advisor Dr. Jannick Rolland, for being a constant source of support and encouragement right from the beginning of my application process to the completion of my Masters research and thesis. I thank her for helping me channel my thoughts and ideas, for her insights and constant feedback, and for steering me in the right direction, facilitating the completion of my thesis research. Having had no formal background in Optics, I also sincerely thank her for her time and patience in teaching me the fundamentals of geometrical optics.

Special thanks to Drs. Shin-Tson Wu, James Harvey, and Kevin Thompson, Vice President of Optical engineering services at Optical Research Associates (ORA) for serving on my committee and to Dr. Shin-Tson Wu and his team for the discussions on liquid crystal technology. I would also like to thank Dr. Yonggang Ha for his assistance with using CodeV™. I thank Dr. Vesselin Shaoulov, former ODAlab team member, for the numerous conceptual reasoning sessions and clarifications during the concept stage of the design. My sincere thanks and appreciation to Dr. Jeff Hoffman of ORA for his valuable time and contribution towards helping set-up the tolerance analysis macro for my system design. My thanks to Dr. Julie Bentley of Tropel Corning, Rochester, NY, for her suggestion of the reflecting microscope objective during our initial stages of research.

I would like to thank my ODAlab team members, especially Anand Santhanam and Ozan Cakmakci for their time and help, be it with subject-related matter or computer support,

and for the interesting debates and conversations. I would like to express my deep and sincere thanks to my friends and fellow students at CREOL, Pradeep Srinivasan, Mahesh Pitchumani and Martina Atanassova for always being there to lend a hand, and for the frequent intuitive discussions and intellectual exchanges. I also deeply thank all my friends for their support and goodwill.

Finally, I thank my parents, Lakshmi and Murali and my sister Divya, for all their prayers and good wishes that have helped me sail smoothly through my work. I am indebted to them for being a constant source of support, for their faith in my abilities and for the inspiration and confidence they have given me.

## TABLE OF CONTENTS

LIST OF FIGURES .....	viii
LIST OF TABLES .....	ix
CHAPTER 1 – INTRODUCTION .....	1
CHAPTER 2 – OPTICAL COHERENCE TOMOGRAPHY- BASIC PRINCIPLE AND BACKGROUND .....	6
2.1 BASIC SCHEME- Time domain OCT .....	7
2.2 Dynamic focusing .....	9
2.2 Goal and Research Methods .....	12
CHAPTER 3 – DEFINITION OF THE IMAGING PROBE .....	13
3.1 System Layout for the Imaging Probe .....	14
3.2 Determination of First Order Parameters for the Microscope Objective.....	16
3.2.1 Functional description of each element in the probe .....	17
3.2.2 First order layout – Computations and Analysis.....	21
CHAPTER 4 - DESIGN OF THE MICROSCOPE OBJECTIVES .....	29
4.1 The Reflecting Microscope Objective .....	29
4.1.1 Starting point and first order layout .....	30
4.1.2 Optimization of the Reflecting Objective design.....	33
4.1.3 Optimized Design and Performance Analysis .....	35
4.2 Refracting Immersion Microscope Objective.....	39

4.2.1 The starting point: An immersion refractive microscope objective without zoom.....	42
4.2.2 Simulating axial resolution – Zoom configuration and dynamic focusing element.....	45
4.2.3 Tolerancing the System.....	51
CHAPTER 5 - CONCLUSION AND FUTURE WORK.....	55
APPENDIX A : CARGILLE LABS IMMERSION GEL 0607 .....	57
APPENDIX B: TOLERANCES AND PERFORMANCE SUMMARY .....	59
LIST OF REFERENCES .....	64



## LIST OF FIGURES

Figure 2.1: Typical <i>En-face</i> OCT setup. (reproduced from: Izatt <i>et al.</i> , 1994) .....	8
Figure 2.2: Different schemes that incorporate dynamic focusing .....	10
Figure 3.1: Design of a dynamic focusing probe .....	14
Figure 3.2: Analysis of a single high NA lens-why it doesn't work.....	17
Figure 3.3: Microscope objective, field Lens, and microlens array subsystem.....	19
Figure 3.4: Collimation lens and MEMS subsystem .....	20
Figure 3.5: Determination of NA of the system. ....	22
Figure 3.6: Raleigh criterion for resolution of two points .....	23
Figure 3.7: Field lens + Micro-lens array subsystem – First order parameters .....	26
Figure 3.8: First-order layout of the collimating lens and MEMS mirror subsystem.....	27
Figure 4.1: Ealing reflecting objective model 25-0506 .....	32
Figure 4.2: Paraxial Layout of the starting point for the reflecting objective.....	33
Figure 4.3: Layout of the final system design with aspheric mirrors .....	35
Figure 4.4: MTF plot for the reflecting microscope objective.....	36
Figure 4.5: Ray aberration plot. ....	37
Figure 4.6: Astigmatism and distortion .....	38
Figure 4.7: Variation of brightness with numerical aperture .....	40
Figure 4.8: Source power spectrum used for system performance analysis. ....	42
Figure 4.9: Preliminary design: lens layout (Top) and MTF (Bottom) at 100 cycles/mm	44
Figure 4.10: Defining a Wood lens (Gradient index lens with a radial index gradient)...	46
Figure 4.11: Lens layout of final design in zoom positions 1, 2 and 3.....	49
Figure 4.12: MTF at the three zoom positions.....	51

## LIST OF TABLES

Table 3-1 Determination of F-number of the microlens.....	25
Table 3-2: Determination of F-number of field lens.....	26
Table 4-1: Specification of Ealing microscope objective – model 25-0506.....	31
Table 4-2: Refractive objective - design specifications.....	41
Table 4-3: First order parameters of the system. ....	48
Table 4-4: Tolerance limits for different cost categories-adapted from K.P Thompson and L.Hoyle, 1994 [47].....	52
Table 4-5: Defined tolerance limits –Select cost category .....	53

## CHAPTER 1 – INTRODUCTION

For several centuries, the microscope has been considered by scientists and physicians to be the ultimate tool for understanding the origins of the disease since it allows imaging of tissue and microstructures in exquisite detail. While microscope technology has evolved, enabling better resolution of smaller anatomical structures, body tissue must still be excised from the body for examination through the microscope. The world's two most fatal diseases, heart disease and cancer, are thought to originate at the cellular level in the thin cellular layer covering the inner and outer surfaces of the body called the epithelium. Understanding these diseases on the microscopic level *in vivo* could lead to better diagnosis and earlier, more precise treatments. Attempts towards such a non-invasive procedure have met with limited success because of two primary reasons: the large size of the diagnostic probe and the poor resolution of the images that are obtained. Presently available external microscopic imaging methodologies like magnetic resonance, X-ray, ultrasound, and nuclear imaging, as well as conventional endoscopy have not been comparable to excisional biopsy, either because of high costs, safety issues, poor resolution and limited penetration, or technical imperfection.

OCT, a novel imaging technique based on low temporal coherence interferometry, has demonstrated the ability to image microscopic structures in biological tissues at sub 10 um resolution and at depths beyond the scope of conventional endoscopy and confocal microscopy [1]. When fully exploited, the technology has the potential to dramatically change the way medical practitioners, biologists, and engineers examine, study, and understand the human body.

As the technology matures, it may be possible to perform optical biopsies using OCT imaging alone, therefore completely eliminating all risk factors involved with excisional biopsy.

The first application of OCT was in a non-medical field where it was employed to find faults in fiber-optic cables [2]. Thereafter, it has been used in other non-medical applications such as industrial metrology, thickness measurement in thin films, non-destructive evaluation of paint etc. [3]-[5]. However, the advantages offered by OCT are exploited to their maximum in its medical applications. The benefits of using OCT are significant in areas where conventional biopsy is ineffective (for e.g., early invasive cancer diagnosis that has high false negative rates), or impossible (biopsies involving the brain, heart, and cartilage surface of bone joints). Another area where OCT will make a major contribution is in the guiding of microsurgical procedures.

OCT enables very high probing depths approaching 2cm in transparent tissue, like the eye. Therefore, ophthalmology is currently the dominant commercial application of biomedical OCT. The first commercial instrument was introduced for ophthalmic diagnosis (Carl Zeiss Meditec AG). Recently, ultra-high resolution techniques have been demonstrated [6], [8] for optical biopsy, thus enabling assessing of tissue and cell morphology *in situ*. One important application of high resolution OCT is in the field of gastroenterology [9], [10]. Dermatology is a second application where high resolution is a key issue [11]-[13].

OCT is ideal for endoscopic imaging of internal organs because of its unique property that depth resolution is decoupled from transverse resolution. The first endoscopic imaging system based on OCT for internal optical biopsy was introduced by Tearney *et al* [14] in 1996. In its cardiac

application, the intracoronary endoscopic OCT has demonstrated a clear differentiation of the different layers of the artery wall. New cardiac research indicates that unstable plaques - arterial lesions that do not constrict the blood vessel but rather burst releasing a bolus of lipids into the blood stream -may be responsible for up to 70 percent of all heart attacks. Plaques and calcifications have been identified and unstable plaques have been clearly distinguished from stable plaques using OCT [15], [16]. Polarization-sensitive OCT has proven to be very useful in dentistry where high birefringence is observed between the enamel and dentin layers of the dental tissue [17]. While OCT has the potential to be used for a variety of medical applications, cancer represents one of the most pressing and promising application areas.

Cancer is a major public health problem in the United States and other developed countries. According to the American Cancer Society (ACS), currently one in four deaths in the United States is due to cancer. One in five Americans will get skin cancer in the course of a lifetime. One person dies every hour from skin cancer, primarily melanoma. More than one million cases of Non Melanoma Skin cancer (NMSC), are found in this country each year. The incidence of the deadliest form of skin cancer, melanoma, is rising faster than that of any other cancer. By 2010, melanoma is projected to rise to one in fifty Americans. Nationally, there are more new cases of skin cancer each year than the combined incidence of cancers of the breast, prostate, lung, and colon. More than 1 million cases of basal and squamous cell skin cancer, approximately 58,490 cases of breast carcinoma in situ and 46,170 cases of in situ melanoma are expected to be newly diagnosed in 2005. It is estimated that more than 85 percent of all cancers originate in the epithelium, the topmost layer of skin.

Early detection of cancerous cells in the skin helps reduce the cost of health care within the US and worldwide. Excisional biopsy is the proven standard method for cancer detection. However, many biopsies are done on a hit or miss basis because only small pieces of tissue are excised at random and dissected to check for cancerous cells. Moreover, excisional biopsy imposes problems like the risk of cancer cell spreading, infection, and hemorrhage. A non-invasive procedure would increase patient compliance for screening for skin lesions since it eliminates the need for numerous evaluations and painful biopsies, thus allowing diagnosis of skin cancer in its early stages when there are better chances of battling the disease. In the quest for a low-cost, non-invasive, reliable imaging system, OCT has come into focus in the last two decades as an effective solution. OCT can greatly improve conventional biopsy by more precisely identifying the areas to be excised based on images of the epithelial layers thereby reducing the number of biopsies and making earlier and more accurate diagnosis possible.

Skin is a highly complex, inhomogeneous, and highly scattering tissue OCT skin imaging has been found to provide a penetration depth in skin that covers the epidermis as well as the dermis (corresponding to approximately 2 mm in skin tissue), which is normally sufficient for detection of skin cancer cells [11]-[13]. Research has shown that typical OCT patterns can be distinguished for different sub-surface skin structures and pathological processes.

The main motivation behind this thesis is to develop an imaging probe that will provide high resolution three dimensional images of the epithelium for non-invasive diagnosis of skin cancer. In the following chapter, the background and principles of the OCT imaging technique are laid out. Specific problems encountered in high resolution OCT are analyzed and previous research to

maintain high resolution throughout the sample scan is reviewed. This thesis concentrates on the design of microscope objectives for dynamic focusing OCT skin imaging probe. The conception and overall design of the microscope probe are outlined in Chapter 3, where the function and description of each component in the probe are laid out. A basic first-order layout is constructed and an effective set of starting paraxial parameters are estimated. Subsequently, the required specifications for the microscope objective are derived and listed. Chapter 4 reports on the detailed design process of two different objective designs that were conceived in order to meet the specifications. The designs were constructed and analyzed using lens design optimization software. A tolerance analysis was also conducted to evaluate the sensitivity of the system to possible errors during manufacture. In conclusion, the benefits and drawbacks of the systems, as well as proposed future work are discussed.

## **CHAPTER 2 – OPTICAL COHERENCE TOMOGRAPHY- BASIC PRINCIPLE AND BACKGROUND**

OCT imaging was pioneered by Professor James Fujimoto, Eric Swanson and their colleagues at MIT and is only a few decades old. OCT imaging can be performed over approximately the same distance as a biopsy at high resolution. The real-time aspect of OCT makes the most attractive applications for OCT those where conventional biopsies cannot be performed or are ineffective. Its roots lie in early work on white light interferometry that led to the development of optical coherence-domain reflectometry (OCDR) [2], a one dimensional optical ranging technique. It was originally developed for finding faults in fiber optic cables [8] and network components. Its potential for medical applications was soon recognized and researchers began to investigate its ability to probe biological tissue structures [18], [19]. While probing depths exceeding 2cm have been demonstrated in transparent tissues, in highly scattering media such as the skin, images are typically obtained as deep as 1-2mm [11]-[13], [18]-[22].

OCT is analogous to ultrasound, but uses near-infrared light as opposed to acoustic radiation, and measures the echo time delay and magnitude of backscattered light [23]. While standard electronic techniques are adequate for processing the high frequency ultrasound technology, which is the current clinical technology with the highest resolution, in OCT interferometric techniques are required to extract the reflected optical signals from the infrared light illuminating the sample. The OCT device typically consists of a Michelson interferometer illuminated by a broadband source. The sample arm light is introduced to a sample by a low numerical aperture lens, while the reference arm mirror scans the sample. The interferometer output is then



processed to produce high-resolution, real time, cross sectional or 3-dimensional images of the tissue. In addition to providing high resolution for the evaluation of micro-anatomic structures, OCT is also inherently able to extract information regarding tissue composition from the spectral absorption characteristics of the specimen [24]-[26].

### **2.1 BASIC SCHEME- Time domain OCT**

In a typical OCT setup a low-coherence broadband light source illuminates the sample through a standard Michelson interferometer. Two scans have to be performed in standard OCT. The lateral OCT scan addresses the laterally adjacent sample positions whereas the depth scan synthesizes images from different depth positions in the sample by performing a series of laterally adjacent time-domain Low Coherence Interferometry (LCI) depth-scans.

The traditional OCT set-up is based on the reflectometry LCI principle [1], which is the most straightforward case of LCI scanning, performed with a Michelson interferometer. In order to improve depth measurement precision, dual-beam OCT has been developed [27]. However, the most commonly used configuration in recent years is *en-face* OCT (see Fig. 2.1), which was introduced by Izatt *et al* (1994). In this implementation a fast lateral scan is performed either by moving the probe beam or the sample, and several such lateral 2-dimensional sections are obtained by adjusting the reference mirror in the interferometer [28]. LCI differs from classical interferometry in that it measures absolute distances. Fringes are formed if the optical path difference between the reference and sample beams fall within the round-trip coherence length  $l_c$  of the beam, called the coherence gate. It is important to note that backscattered light travels

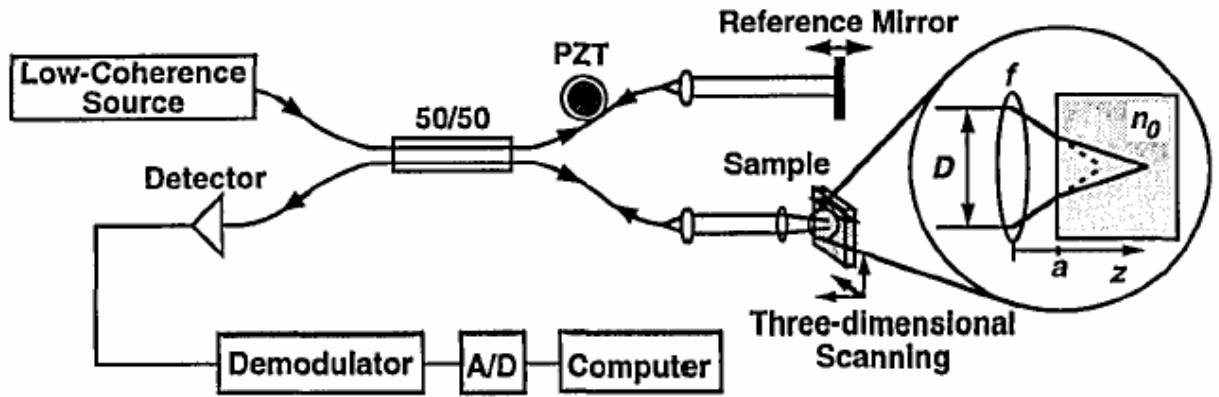


Figure 2.1: Typical *En-face* OCT setup. (reproduced from: Izatt *et al.*, 1994)

twice through the sample. The coherence gate  $l_c$  is used as an estimate of the depth resolution of the OCT system and assuming a Gaussian source spectrum it can be expressed as

$$l_c = \frac{2 \ln 2}{\pi} \frac{\bar{\lambda}^2}{\Delta \lambda} = \frac{l_{FWHM}}{2} \quad 2.1$$

where  $\bar{\lambda}$  is the mean wavelength,  $\Delta \lambda$  is the spectral width, and  $l_{FWHM}$  is the full width at half-maximum of the Gaussian source spectrum. The transverse resolution is measured from the size of the focused image spot as given by

$$\delta r = \frac{4 \bar{\lambda}}{\pi} \frac{f}{d} \quad 2.2$$

where  $f$  is the focal length of the objective and  $d$  is the beam diameter on the objective. The generalization to a non-gaussian spectrum has also been investigated by Avni *et al* [29]. OCT has several outstanding properties. First, depth resolution is independent of transverse resolution as can be surmised from Equations 2.1 and 2.2. This property allows for high depth resolution while imaging structures that do not permit high lateral resolution since they are not accessible using high numerical aperture (NA) beams. If high NA beams are used, however, high lateral resolution is also achieved; this is then called Optical Coherence Microscopy (OCM). Second,

depth resolution is in the nearly histological 1 $\mu$ m regime. Third, this technique provides high sensitivity, greater than 100dB [30], enabling imaging of weakly scattering structures like in the case of *in situ* optical biopsy. Lastly, this technique is non-invasive and can yield *in vivo* data [1].

OCT does have two major drawbacks. A depth-scan needs to be performed, a problem that can be resolved using the recently developed Fourier-domain OCT [31], [32]. Moreover, time-domain OCT operates on a point-to-point basis. The latter can be avoided by employing a relatively new technique called parallel OCT [33], [34].

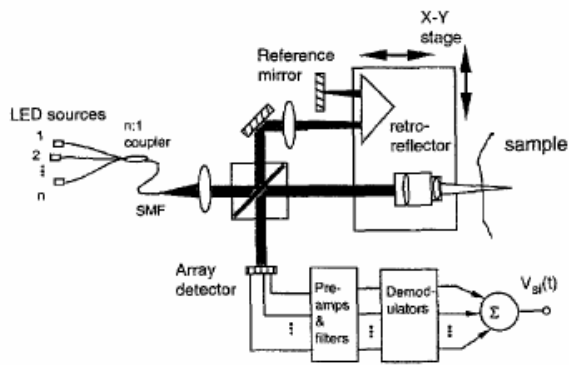
## **2.2 Dynamic focusing**

A specific problem that can arise in OCM and high-resolution OCT is the depth dependence of transversal resolution. The depth of focus (DOF) can be expressed as twice the confocal beam parameter of a Gaussian beam as follows:

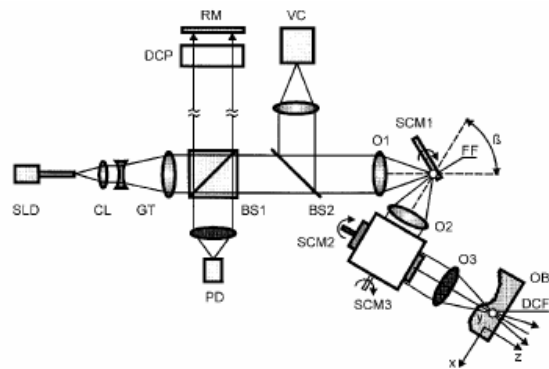
$$DOF = 2 \frac{\bar{\lambda}}{\pi \bar{\theta}^2} \quad 2.3$$

where  $\bar{\theta}$  is the angular spread of the beam and is inversely related to the transverse resolution  $\delta r$  [30]. Hence for high lateral resolution, a large angle  $\bar{\theta}$  is required. A large angle  $\bar{\theta}$  implies a large NA which gives rise to a small confocal beam parameter and consequently a small depth of focus.

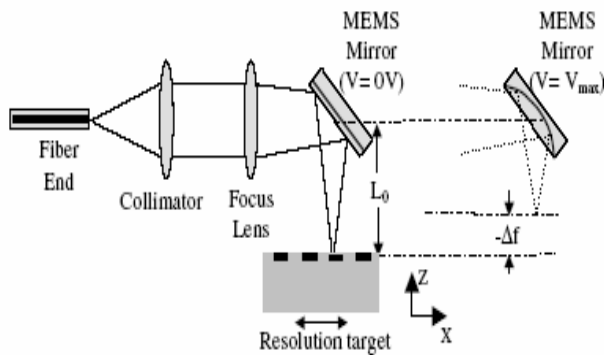
One means of ensuring invariant resolution throughout both the axial and lateral scans is via the use of a dynamic focusing system. Schmitt *et al* first described a system that dynamically focused inside the sample by the use of a common transition stage for both the imaging objective



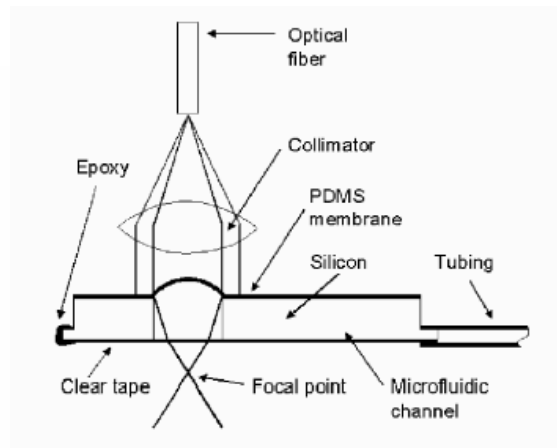
(a) Schmitt *et al.* (1997)



(b) Lexer *et al.* (1999)



(c) Qi *et al.* (2004)



(d) Divetia *et al.* (2005)

Figure 2.2: Different schemes that incorporate dynamic focusing

and a retro-reflector used in the reference depth scan, thereby mechanically moving both the reference and sample arm in synchronicity [35]. In order to enhance depth resolution, multiple sources are simultaneously used to synthesize a very short temporal coherence length. Such a system or its equivalent is now in widespread use in laboratory experimental work [36].

A few other methods have thereafter been developed to implement dynamic focusing and high resolution 3D imaging. In an ideal OCT system, scanning of the reference length and sample

beam would require no moving parts at all. Lexer *et al.* suggested the use of an optical setup where the sample is moved for each depth scan while the arms of the interferometer remain constant. In this method, an oscillating beam focus formed through reflection from an oscillating mirror is axially magnified  $M$  times by lenses before illuminating the sample. At each discrete point of the oscillation, the optical path difference caused because of the oscillating beam focus first formed causes a corresponding dynamic shift in the beam focusing in the sample. The path length traveled within the sample, however is altered by the refractive index of the sample and this causes a depth of sample to be imaged corresponding to the amplitude of oscillation [37]. Drexler *et al.* investigated an alternative to dynamic focusing called zone focusing [6]. In this technique, individual layers in depth are imaged, each depth with a new focusing of the beam in that layer. An image fusion technique is then used in which tomograms from different layers are fused to form a 3D data set. This technique is similar to C-mode scanning used in ultrasound imaging. More recently, B. Qi *et al.* have proposed a high-speed dynamic focus control system based on a microelectromechanical (MEMS) mirror that is deformable. The MEMS mirror shifts the focus position of the sample beam to match with the coherence gate position for each lateral scan [38]. With this design, dynamic focusing is achieved at high speeds since it does not involve bulk optics. An alternate method was proposed by A. Divetia *et al.* where the OCT probe was designed to have a built-in dynamic focusing ability by the addition of a liquid-filled polymer lens whose curvature is controlled by variation of the hydraulic pressure in the lens. The latter system required no moving parts [39].

## **2.2 Goal and Research Methods**

The ultimate goal of our research is to develop a tunable focus bio-photonics probe for detecting and quantifying abnormal cells in cultured skin models using OCM. The size of cells in animals and humans is typically of the order of 5-10 $\mu$ m. Our OCM system has therefore been configured to resolve to a lateral resolution of 5 $\mu$ m. In order to preserve this resolution throughout the depth of scan, we have developed a dynamic focusing system to perform multiple 2D *en-face* scans at various focal depths of the tissue. We use a Ti-Sapphire laser source spectrum for our probe design and experimentation. This was because for high-resolution dynamic range OCT, one of the most suitable light sources is the Kerr-lens mode-locked Ti-Sa laser that has been demonstrated to have a wavelength range of 0.7 to 1.1  $\mu$ m with a mean wavelength of approximately 800 nm [40]. The skin probe has been designed for time-domain OCT but can be easily adapted to Fourier-domain OCT if the applications so demand.

## CHAPTER 3 – DEFINITION OF THE IMAGING PROBE

We present the design of a hand-held skin imaging probe that can dynamically focus in skin *in vivo*. The novelty in the approach lies in combining emerging micro optical elements technology, tunable lenses, and MEMS mirrors for large sample and high-resolution imaging.

The probe was designed to perform imaging of a 2mm in depth by 2mm lateral skin sample at a resolution of 5 $\mu$ m or less. The probe design may with be integrated a single-axis or dual-axes MEMS for 2D or 3D imaging, respectively. The MEMS enables the scan along the skin in either the x or y lateral dimensions. Scanning the reference arm enables the depth or z-scan, which in the case of this probe will be synchronized with the dynamic focusing in the sample arm. Ideally, the ultimate objective is to obtain video rate (30 frames/sec) high resolution imaging together with sample sizes of a few millimeters. At smaller samples of (50-100  $\mu$ m lateral dimensions and less than 1.5 mm in depth) which are typically demonstrated in current high resolution imaging does not enable optimal detection and characterization of skin [6], [41].

In this chapter, the overall probe design is laid out to meet the specifications of fine lateral resolution at large sample depth. The different probe components, their primary function and contribution, and the determination of first order starting parameters for the microscope objective will be discussed.

### 3.1 System Layout for the Imaging Probe

The design of the tunable-focus probe was developed from basic principles of optical instrumentation and the probe layout is illustrated in Fig. 3.1. The first-order layout of the dynamic focus skin imaging probe comprises a microscope objective, a field lens, a microlenslet array, collimation optics, and a MEMS scanning mirror. Dynamic focusing in this layout may be accomplished using one of two approaches. In the first approach, the microscope objective is chosen to be an achromatic, all-reflective design that is not tunable. The microlenslet array, on the other hand, is made of tunable microlenses. In the second approach, the microscope objective is made of tunable microlenses. In the second approach, the microscope objective is designed to be an all-refractive system and the dynamic focusing element is incorporated within the objective. In the latter case, tunability is achieved within the microscope objective and the microlenslet array does not require tunability.

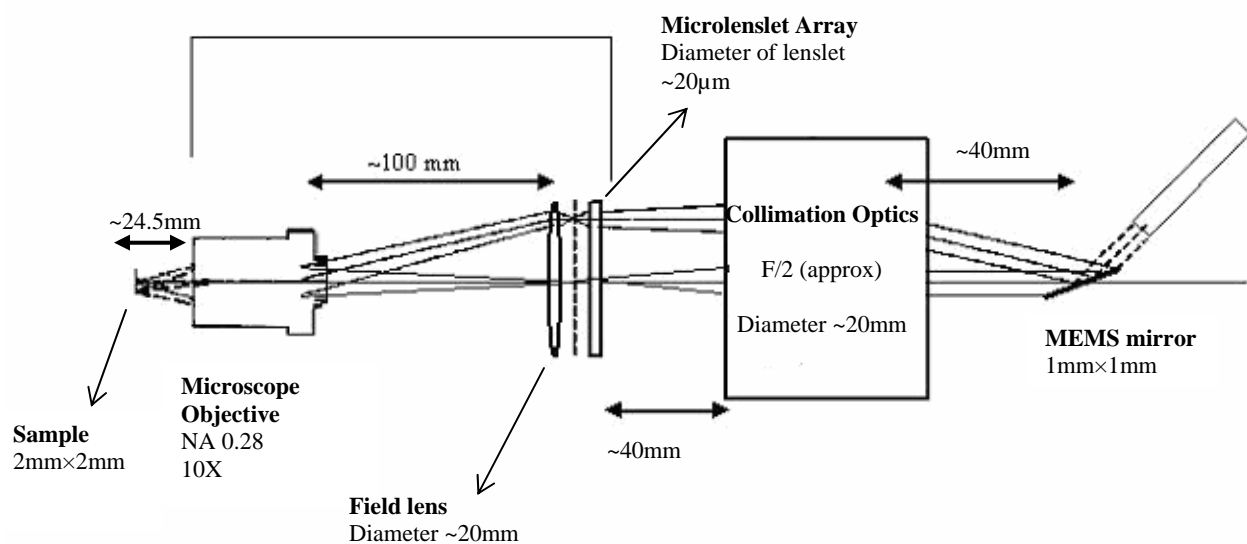


Figure 3.1: Design of a dynamic focusing probe



One solution to the problem of dynamic focusing, which is the solution we have explored for both approaches reviewed above, is the use of liquid crystal (LC) micro-optics tunable-focus optics in order to enable axial scan at quasi-uniform resolution. The key in using LC technology is that its transmission remains constant over the optical spectrum, including IR. It is important to know that for liquid crystal tunable optics, the smaller the optics the easier it is to tune. This property guided us in the two designs of the probe. However, a lower limit in size is imposed by diffraction, which will induce some light loss.

In the first configuration with the all-reflective microscope objective, the field lens and microlenslet array subsystem require self-motion within the probe. Such motion can be accomplished using a piezoelectric pump in which the user holds the overall probe fixed with respect to the skin. This design was conceived in collaboration with Dr. Quanfang Chen at the University of Central Florida and is only summarized here as a pointer to overall system design. A collar is used for mounting the moving components, while the non-moving optical components are mounted within the shaft. The collar is linked to a miniature pump, which is driven by a smart material (i.e., piezoelectric) and is integrated with microvalves. These microvalves possess precisely controllable flow rates that allow the system to realize a motion resolution down to the nanometer range. In this design, the MEMS and collimation optics remain fixed throughout the dynamic focusing and the LC microlenslet arrays adjust their focal length to allow light from various imaging depths to be coupled back into the interferometer. Only the microscope objective, field lens, and microlenslet array subsystem need to move by a small amount to compensate for the change in the position of the image formed by the microlenslet array at each depth  $z$ . The motion of the subsystem is necessary because the collimation optics that follows the

subsystem stays stationary and its design has been targeted to operate at fixed conjugates. The size of the microlenslets is given by half the lateral resolution in air ( $2\mu\text{m}$ ) times the lateral magnification of the microscope-field-lens assembly. To obtain  $4\mu\text{m}$  effective resolution in air we must sample at  $2\mu\text{m}$  intervals according to the Raleigh sampling criterion. The Numerical aperture of 0.28 is set by the Optical Lagrange Invariant and the diffraction Airy disc diameter as illustrated in Section 3.2. The image through the microlenslets must be located at the focal plane of the collimation lens (for example, 50 mm, F/N, where N can be anywhere between 2.5 and 5).

Alternatively, in the second configuration with an immersion refractive microscope objective, a tunable-focus LC lens is incorporated within the microscope design in order to dynamically refocus at various depths of skin. This completely eliminates the need for the liquid crystal element in the microlenslet array. Also, since the liquid crystal element changes the effective focal length of the refracting objective such that the image distance is always constant, it eliminates the need for any moving parts. This configuration, although more complicated, provides for a more robust design. The lack of mechanical motion in this system increases accuracy, the repeatability of measurements, and the scanning speed. Except for the fact that the microlenslet array is not addressable or tunable, the general probe layout for this system remains the same as for the previous case.

### **3.2 Determination of First Order Parameters for the Microscope Objective**

The first order starting parameters were laid out based on the constraints, requirements and feasibility of manufacturing of each element of the probe. In this section, we first discuss the

function of each element or subsystem of the probe and how it affects the rest of the design. Next, the numerical computations and analysis resulting in first-order starting parameters for the components of the probe are explained. Once the general overall first-order probe setup is laid out, we come to a conclusion on the optimal magnification and numerical aperture for the microscope objective to be designed.

### 3.2.1 Functional description of each element in the probe

In this sub-section, we will discuss the functions and purpose of the microscope objective, microlenslet array, field lens, collimation optics, and the MEMS mirror. In order to address the question that arises regarding the need for so many components, let us first consider a simple imaging system that consists of a single lens combined with a MEMS.

Why won't a single high-numerical aperture lens work? Such an idea could be conceived in the telecentric mode with the object at the focal point of the lens and the MEMS at the focal

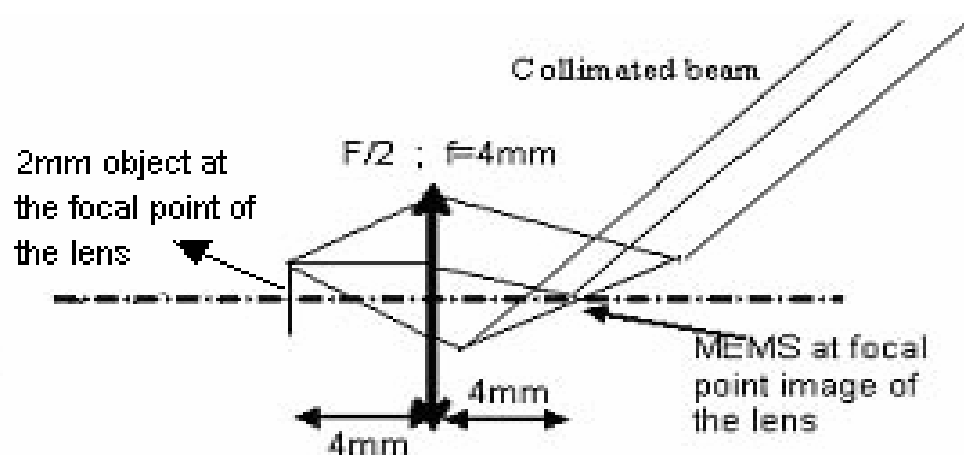


Figure 3.2: Analysis of a single high NA lens-why it doesn't work

point image of the lens as shown in Fig. 3.2. For example, to achieve a resolution of  $2\mu\text{m}$  at  $800\text{nm}$  requires a NA of 0.25 or a lens of F-number approximately equal to 2. It is well known within the science of lens design that F/2 lenses are always challenging to design, especially for a broadband spectrum. However, this is not the reason it does not work. If the sample is  $2\text{mm}$  laterally, and the lens is a few millimeters, then the focal length scales accordingly. Let, without loss of generality, the lens diameter  $D$  be  $2\text{mm}$  and thus  $f$  be  $4\text{mm}$ . The geometry shown sets the size of the scanning mirror to be approximately the size of the beam at the lens (i.e.  $D$ ) divided by  $\sin(\theta)$ , where  $\theta$  is the minimum tilt of the MEMS. Therefore, such design requires a very large MEMS mirror as shown from geometry. Large sizes (beyond  $1\text{mm}$ ) do not allow for high speed scanning and hence, such solution is not viable. This justifies the need for a more effective imaging system that addresses these issues. A comprehensive imaging probe was conceived to meet the requirements with the following functional components.

**Microscope Objective:** The primary function of the microscope objective is to magnify the sample being imaged. The key advantage of using an all-reflective design in the first configuration was the lack of chromatic aberrations for high numerical aperture optics. This design was ideal in terms of its size and weight and was the objective of choice for the probe model that had a tunable microlenslet array. In the second scheme, we chose to use a refracting microscope objective with a dynamic focusing element as discussed previously. In both cases, the magnification of the objective is limited by the following factors: size of the sample ( $2\text{mm}$ ), minimum resolution ( $4\mu\text{m}$ ), minimum diameter of the lenslets that can be fabricated, and maximum diameter of the probe that still allows it to be hand-held.

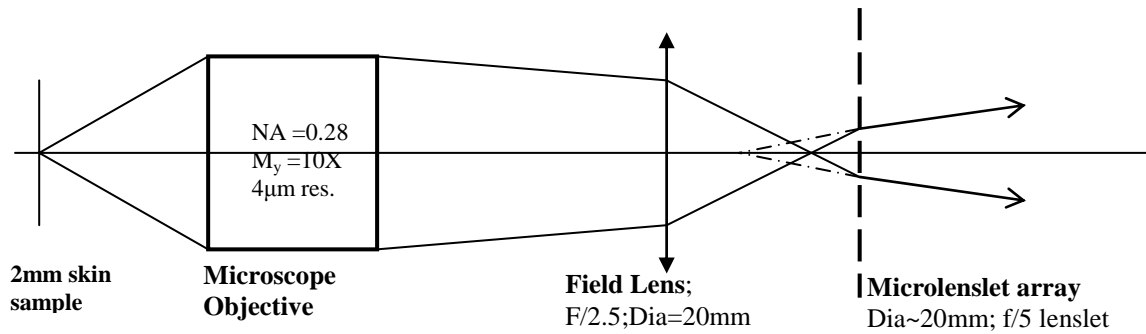


Figure 3.3: Microscope objective, field Lens, and microlens array subsystem

**Field Lens:** The primary function of the field lens is to modify each off-axis beam emerging from the microscope objective from every sample point into a telecentric beam for the microlenslet array. The field lens is positioned very close to the image point of the microscope objective and hence has a magnification of approximate unity and does not significantly alter the incoming beam otherwise. However, it has several advantages for the system. First, it helps reduce the beam size and consequently the microlenslet array diameter. Second, it collimates the chief ray from each sample point in the lateral scan, thus eliminating off-axis aberrations for the microlenslet array.

**Microlenslet Array:** The primary function of the microlenslet array is to place the image formed by the field lens at the focal plane of the collimation optics. Each lenslet has a focal length on the order of microns owing to its size, and therefore, it helps shorten the length of the system. The microlenslet array can have a relatively large F-number, for example, F/5 or F/10. The object size, magnification of the objective, as well as the F-number of the microlens will determine the focal length of each microlens. The microlenslet array is positioned after the field lens so that it

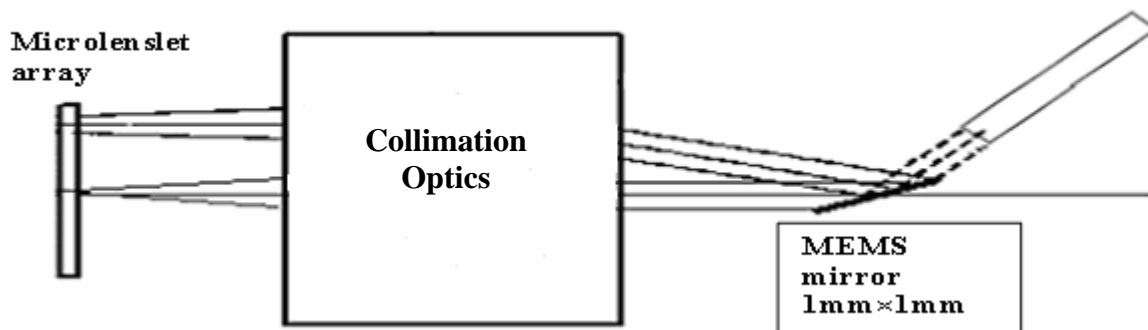


Figure 3.4: Collimation lens and MEMS subsystem

forms a virtual image. In other words the field lens image has to fall within the focal point of the microlens. This will help to further minimize the length of the probe.

**Collimation lens and MEMS mirror:** The collimation lens gives a parallel beam that will be re-oriented using the MEMS mirror. The implementation of a lateral scan is done by tilting the MEMS mirror through the required angle. The size of the MEMS chosen allows reasonable scan speed and yet does not require any innovative design in collimating the beam entering the probe. In Fig. 3.4, we show two beams passing through the probe, which are sequential in time. The upper beam corresponds to the MEMS mirror laying flat (0Deg.) while the on-axis beam corresponds to the MEMS at an angle. The MEMS at twice that angle would yield the lower beam (not shown) symmetric with respect to the upper beam. The continuous scan of the MEMS mirror will enable a tilt through all angles that correspond to the 2mm lateral size of the sample at  $2\mu\text{m}$  sampling rate.

### 3.2.2 First order layout – Computations and Analysis

Having laid out the functional significance of each probe component, the first step in determining first order parameters for the system is to determine the numerical aperture of the microscope objective. Fig. 3.5 illustrates the imaging of a 2mm sample with a monochromatic source of 800nm. We have used the thin lens configuration for simplification during first-order analysis. Also, it needs to be noted that we have done the following first-order calculation for a 2 $\mu$ m resolution target, although 4 $\mu$ m resolution is sufficient for skin imaging. The primary reason for this is to take into account aberration effects that do not appear in first order calculations. A second advantage in designing the microscope objective to meet a 2 $\mu$ m resolution specification is to make the system flexible enough for future work, in case it demands much higher resolution for other applications.

The Lagrange invariant gives us the marginal ray angle  $\alpha'$  for the objective as shown in Equation 3.1.

$$n \cdot p \cdot \sin \alpha = n' \cdot p' \cdot \sin \alpha' \quad 3.1$$

where  $p$  and  $p'$  are the object and image half heights respectively,  $n$  and  $n'$  are the refractive indices of the medium in object and image space, and  $\alpha$  and  $\alpha'$  are the entering and exiting marginal ray angles for the objective. If NA denotes the numerical aperture of the objective, given by Equation 3.1 and the lateral magnification  $m_p$  of the objective defined as  $p'/p$ , then the exit angle  $\alpha'$  is very small and Equation 3.1 can be simplified as shown in the following equation.

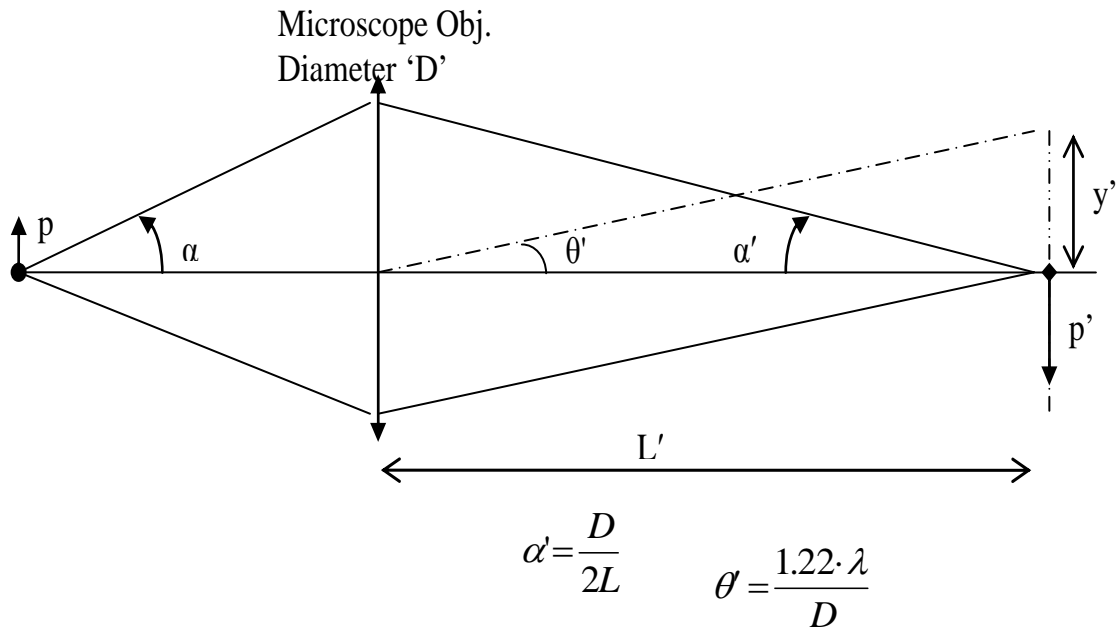


Figure 3.5: Determination of NA of the system.

$$\alpha' = \frac{NA}{m_p} \quad . \quad 3.2$$

Also if  $D$  is the exit pupil diameter, and  $L$  is the image distance,  $\alpha'$  can be expressed as

$$\alpha' = \frac{D}{2L'} \quad . \quad 3.3$$

The diffraction angle  $\theta'$  and diffraction spot radius height  $y'$  are given by Equations 3.4 and 3.5 respectively.

$$\theta' = \frac{1.22 \cdot \lambda}{D} \quad 3.4$$

$$y' = \frac{1.22 \cdot \lambda \cdot L'}{D} \quad 3.5$$

Equation 3.5 simplifies to

$$y' = \frac{1.22 \cdot \lambda \cdot m_p}{2 \cdot NA} \quad 3.6$$



Therefore,

$$y = \frac{1.22 \cdot \lambda}{2 \cdot NA} \quad 3.7$$

The Airy disc radius  $y$  is known to be  $2 \mu\text{m}$ , therefore the NA is determined to be 0.244 at 800 nm. The closest commercially available objective that could be used as a starting point had an NA of 0.28. So the NA of the microscope objective for the skin probe was set to be 0.28 in order to match with preliminary tests conducted with the objective readily available commercially.

The next step was to determine the size and F-number of the microlenslet array and how they relate to the magnification of the microscope objective. The Raleigh criterion was used to determine the sampling frequency needed for a resolution of  $4 \mu\text{m}$ . The criterion states that two points or lines are just resolved if the first peak of one point spread function lies on the first trough of the other point spread function. In other words, the sampling interval has to be at most half of the required resolution. Therefore, for a  $4 \mu\text{m}$  resolution, a  $2 \mu\text{m}$  sampling interval is needed. If the maximum diameter of the lenslet array that would still ensure compactness is approximately 80mm, and a 2mm sample is imaged, then the required magnification of the microscope objective would be around 40X. The size of the microlenslets is given by half the

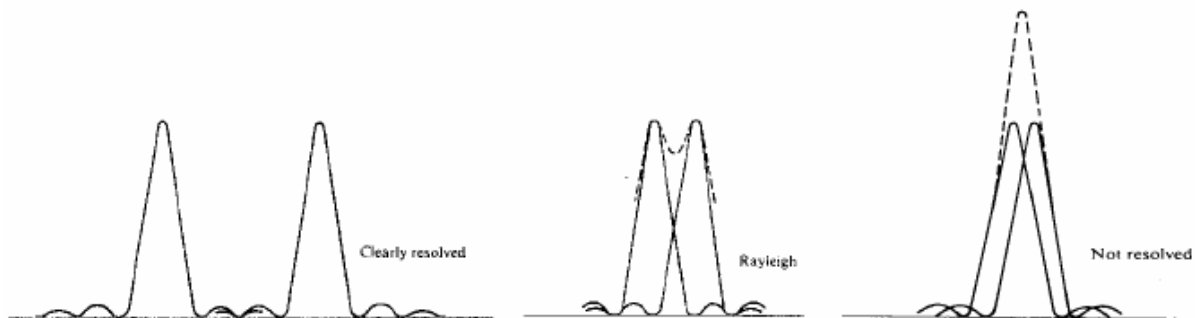


Figure 3.6: Raleigh criterion for resolution of two points

lateral resolution in air ( $2\mu\text{m}$ ) times the lateral magnification of the microscope-field-lens assembly.

The other first-order parameters for the micro-lens are arrived at by estimating the diameter of the blur spot caused by diffraction and spherical aberration of the image formed through the microlens for all possible microscope objective magnifications and microlenslet array diameters. State-of-the-art microlenslet arrays allow for the microlens diameter to be approximately  $10\mu\text{m}$ . So, a 5X microscope objective will just meet specifications for a  $4\mu\text{m}$  resolution criterion. In order to allow some tolerance for error, different microlens diameters corresponding to a range of 10X-40X microscope objectives were investigated. In each of these cases, three different F-numbers were analyzed and the aberration and diffraction blur spots corresponding to each F-number were compared. The blur diameter of the spot caused by spherical aberration (which is the primary source of aberration for the microlens owing to the lack of off-axis beams) and blur diameter of the Airy disc caused by diffraction effects were calculated and compared based on the first order formulae given in Equations 3.7 and 3.8. If  $f$  represents the focal length of the lens,  $\lambda$  the wavelength of the light source (approximately  $800\text{nm}$ ) and  $F\#$  is the F-number of the microlens considered, then the estimate for the diameter of the image blur due to spherical aberration(SA) and diffraction are respectively expressed as

$$\text{Diameter}_{\text{blur}_{\text{due}_{\text{to}_{\text{SA}}}} = \frac{0.067 \times f}{(F\#)^3} \quad 3.7$$

$$\text{Diameter}_{\text{Airy}_{\text{disc}}} = 2.44 \cdot \lambda \cdot F\# . \quad 3.8$$

Both these formulae are derived for infinite conjugates. Since the microlens was intended to produce a nearly parallel beam that reaches the collimator, we assumed the microlens to be a

nearly plano-convex lens. These formulae are therefore useful to make rough estimates of the size of the image formed.

Table 3-1 Determination of F-number of the microlens

$M_y$	40X			20X			10X		
Lenslet Dia ( $\mu$ )	80			40			20		
F#	<b>f/2</b>	<b>f/5</b>	<b>f/10</b>	<b>f/2</b>	<b>f/5</b>	<b>f/10</b>	<b>f/2</b>	<b>f/5</b>	<b>f/10</b>
Focal length ( $\mu$ )	160	400	800	80	200	400	40	100	200
SA Blur Dia ( $\mu$ )	1.34	1.072	0.0536	0.67	0.1072	0.0268	0.335	0.0536	0.0134
PSF Dia ( $\mu$ )	3.904	9.76	19.52	3.904	9.76	19.52	3.904	9.76	19.52

Based on the above figures, it can be concluded that diffraction effects are the primary cause of blur in the spot, when compared to spherical aberration. Since the image quality is not affected greatly by aberration, we have more freedom in choosing the microscope objective parameters. Since in this case, the magnification power of the objective does not contribute to the diameter of the Airy disc that determines the image size, the optimal design was chosen to be a 10X objective. As for the F-number, while an F/2 lens gave us the smallest spot diameter, it was more sensitive to minor error in positioning because of the smaller focal length. An F/5 lens on the other hand offered a longer focal length and was also easier to manufacture and its diffraction blur diameter fell well within the microlens diameter. Therefore, a 10X microscope objective and a 20 $\mu$ m diameter microlens with an F-number of 5 was concluded to be optimal for this design.

The numerical aperture of the microscope objective is 0.28. The Lagrange invariant sets the half height of the image formed by the objective to be 10 $\mu$ m. Suppose the field lens is placed within 3mm of the objective image point such that it sees a virtual object (Fig. 3.7), the F-number of the

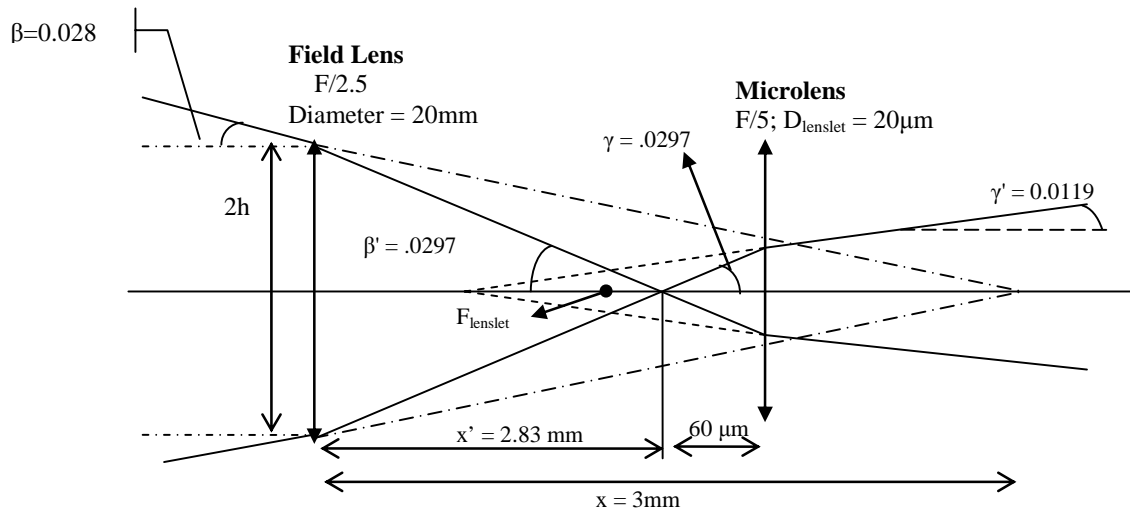


Figure 3.7: Field lens + Micro-lens array subsystem – First order parameters

field lens needs to be set so that the beam converges further. The diameter of the beam reaching the field lens being known, the diameter of the field lens is computed to be approximately 20mm. The image distance and exit marginal ray angle  $\beta'$  were evaluated for three different F-numbers as outlined in the following table 3-2. The distance from the image point at which the beam diameter will fully cover the 20µm diameter microlenslet was calculated. This helped in positioning the microlenslet array such that the entire beam from each sample point is fully received by each lenslet.

Table 3-2: Determination of F-number of field lens.

	F/2	F/2.5	F/5
Image distance $x'$ in mm	2.790	2.830	2.913
Marginal angle $\beta'$ in rad	0.03011	0.02968	0.02884
Distance (in µm) at which beam ht is 20µm	332.143	337.000	346.740

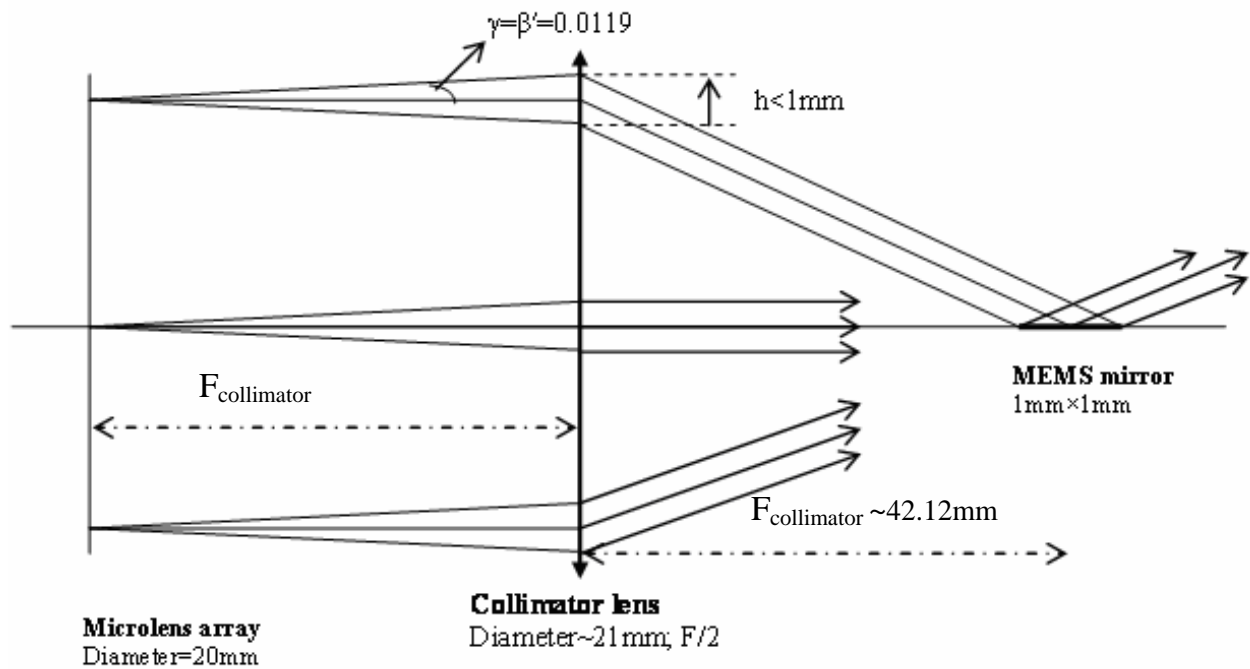


Figure 3.8: First-order layout of the collimating lens and MEMS mirror subsystem.

The F/2 lens was eliminated because it offered no significant difference over the F/2.5 lens. The F/5 lens had too small of an angle  $\beta'$  and constrained the positioning of the micro-lens, whose focal length is in the order of microns. Therefore the F/2.5 field lens is the optimal choice.

In order to arrive at the object distance for the microlens, assume that the micro-lens has an F-number of 5. Its focal length is therefore  $100\mu\text{m}$ . The microlens needs to be placed within the field lens image point such that it forms a virtual image. We evaluated the exit angle  $\gamma'$  of the diverging beam from the microlens at different values of 'x' ranging from  $60\text{-}90\mu\text{m}$ . The largest angle ( $\gamma'=0.011872$  rad) was obtained for a distance of  $x = 60\mu\text{m}$ . The larger the exit angle, the shorter the distance to the collimation optics. Therefore, the object distance for the microlens was chosen to be  $60\mu\text{m}$ .

The MEMS and collimation optics are illustrated in Fig. 3.8. The exit angle from the micro-lens and the diameter of the MEMS mirror (1mm) set the diameter of the collimating lens and its distance from the microlenslet array. As evident from Fig. 3.8, the MEMS mirror and the microlenslet array are both placed at the focal points of the collimation optics. This sets the F-number of the collimation optics to be approximately 2 in the first order paraxial layout. The largest tilt angle needed for the MEMS mirror to pass the lowermost beam is therefore calculated to be -14 Deg.

## CHAPTER 4 - DESIGN OF THE MICROSCOPE OBJECTIVES

The first design in this chapter involves a Reflecting Objective – an objective lens system that has only mirrors of different powers. The main purpose behind using an all-reflecting design is to eliminate chromatic aberrations. Hence this system can be used over a broad spectrum. The main drawback however, is the presence of moving parts in the overall system that was needed in order to enable dynamically refocusing across the sample depth.

The second design is based on an all-refractive configuration that had the dynamic focusing capability as part of the objective. Such a design removes the needs for moving parts and facilitates repeatability and faster measurements.

In Section 4.1, we discuss the first-order layout, modeling, optimizations, and performance of the reflecting microscope objective. In Section 4.2, we present the design, analysis, and the evaluation of the refracting microscope objective.

### **4.1 The Reflecting Microscope Objective**

Reflecting microscopes date back to the invention of the early telescope objectives, since they were just an inverted configuration of a telescope. However, these objectives were severely limited by coma in systems with an NA greater than 0.1. An analytical solution for an aplanatic microscope objective was first investigated by Karl Schwarzschild in 1905, made up entirely of spherical mirrors. It consisted of a small convex primary mirror and a large secondary concave mirror. By choosing the appropriate values for the mirrors' radii of curvature and their

separation, it was possible to correct two of the primary monochromatic aberrations for the system: spherical aberration and coma [43]. However, such a design would fail in large NA systems beyond 0.5, where the design performance becomes severely limited by astigmatism. This was compensated for by the use of aspherics as demonstrated by C.R Burch in 1946 [42].

The primary advantage a reflective system lies in the use of mirrors because of their unique optical property: the absence of chromatic aberrations due to their all-reflecting nature. This design is attractive in terms of its size and weight and is investigated for performance for the probe configuration that has a tunable element incorporated in the microlenslet array. Reflecting objectives also commonly find applications in Fourier transform infrared spectroscopy and microscopy, photolithography, and microsurgery.

#### **4.1.1 Starting point and first order layout**

The first step in any design is the starting point selection, where concepts move toward reality. Often, this step is enhanced with an existing solution for a similar or related situation found in books, patents, or literature. Graphical and approximate methods can also be used to create a starting point if necessary. In our case, we chose a commercially available product that closely matched our design specifications.

Our starting point was an all-reflective microscope objective based on the Schwarzschild configuration available commercially called the Ealing Reflecting objective, model 25-0506. Each standard model is supplied with internal mirrors coated with bare aluminum providing



greater than 89% reflectivity across a large spectrum (250nm – 10 $\mu$ m), which is inclusive of the used spectrum of laser light. This combination is useful in most applications involving low power levels.

The starting point was to obtain the specifications of the Ealing product available in their product catalog. From the available parameters, an approximation was made to estimate the remaining parameters needed as a starting point for our required system. The specifications obtained readily from the product catalog are given in Table 4-1.

Table 4-1: Specification of Ealing microscope objective – model 25-0506.

Magnification	15X
Numerical Aperture (NA)	0.28
Visual Field of View (FOV) in mm	1.20
Effective focal length in mm	13.35
Obscuration %	18.90
Small mirror diameter in mm	7.3
Maximum external diameter in mm	160.0
Approx tube length in mm	46.0

The starting parameters in the design of the reflective optical system were the design specifications of the above 15X Ealing Reflecting Objective. In order to complete the layout, we also needed to determine other preliminary values such as the distance between the mirrors, and the object and image distances in order to complete the basic layout. We estimated the diameter of the concave mirror to be 45.0mm, the distance between the object and the convex mirror to be 24.5mm, the distance between the two mirrors to be 35mm, and the distance between the concave mirror and the image to be 100mm.

Based on these starting values and the required specifications for the microscope objective, calculations were carried out for determining best estimates of the basic parameters such as the focal length and radius of curvature of the mirrors for the first order layout. Using Descartes imaging equation given by

$$\frac{n}{x} + \frac{n'}{x'} = \frac{n'}{f'} \quad 4.1$$

where  $n$  and  $n'$  are the refractive indices in the object (e.g.  $n=1$ ) and image space (e.g.  $n'=-1$ ) for each imaging element,  $x$  and  $x'$  are the object and image distances, and  $f'$  is the focal length.

From the equation for effective power given by

$$\phi = \phi_1 + \phi_2 + \frac{e}{n} \phi_1 \phi_2 \quad 4.2$$

where  $\phi = \frac{n'}{f'}$  represents the power of each surface, the focal lengths and radius of curvature of

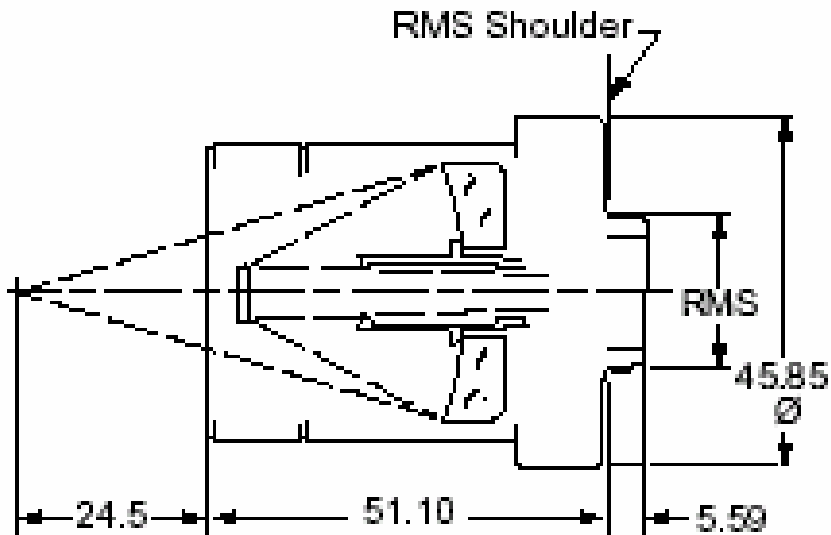


Figure 4.1: Ealing reflecting objective model 25-0506

the two mirrors were obtained. The focal length of the first mirror was found to be 25mm and its radius of curvature 50mm. For the second mirror, the focal length was approximately calculated to be 11mm, and its radius of curvature 22mm. Using ray tracing and the Descartes equation the aperture stop for the above system was found to be the convex mirror. All the paraxial system parameters were thus laid out.

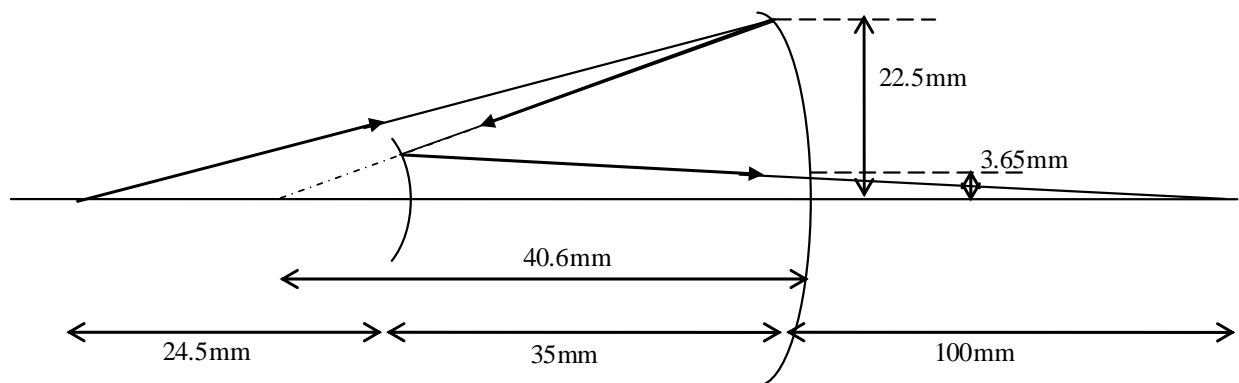


Figure 4.2: Paraxial Layout of the starting point for the reflecting objective

#### 4.1.2 Optimization of the Reflecting Objective design

The paraxial parameters having been laid out, the set of variables such as curvature, thickness, and index of refraction were set to vary within an optimization routine. An error function and constraints that set the boundary values were defined. Initially, a system involving only spherical mirrors was optimized and analyzed following the Schwarzschild configuration discussed previously. In order to ensure better resolution and contrast, the mirror surface properties were subsequently changed to be aspheric in the final reflecting objective design. The 4<sup>th</sup>, 6<sup>th</sup> and 8<sup>th</sup> order coefficients of the asphere and also the radii of curvature of the aspheric surfaces were varied and optimized.

The configuration was inverted for easier optimization using CodeV™, since the lens design tool performs better when operating from longer conjugates to shorter conjugates (See Fig. 4.3). For a 4 micron resolution, the cut-off frequency for the MTF at the image plane was found to be 250 lp/mm. In other words, at this spatial frequency on the image plane/detector, we set our desired target MTF to be 30% or higher. Since there are no chromatic aberrations in an all-reflective system, the optimization was carried out at a single wavelength of 587.56nm. The system however will function similarly at any given frequency.

The error function for this system was minimized in automatic design using the default CodeV™ error function construction, which is basically a center-weighted RMS spot size, weighted for wavelength, aperture, field, and zoom position. It is typically calculated for each field and zoom position from a grid of rays traced in each wavelength. Ideally, the error function value would be 'zero' which would imply a perfect image. The ray grid is determined by the value of DEL, which defines the ray spacing in a pupil of normalized radius 1. For systems with non-spherical surfaces, the default value of DEL is automatically adjusted to provide a 34 ray pattern in the half pupil. This applies to the considered system since it has aspheric surfaces. The denser ray grid assures that the variation in the surface profile was sampled with higher resolution in order to better represent the effect of the surface. The next step was to optimize the lens

### 4.1.3 Optimized Design and Performance Analysis

Results of the optimization carried out for the Schwarzschild design (not shown here) demonstrated that it was primarily limited by Petzval curvature and did not meet the required MTF specifications for the required FOV. Changing the mirror surface properties to be aspheric helped the overall MTF as a result of an improved balancing of aberrations and thus yielded an increase in image resolution and contrast. Significant improvement in MTF was observed over the Schwarzschild setup for a large field of view. However the lens was still limited by Petzval curvature.

The plots in Fig. 4.4, 4.5, and 4.6 demonstrate the results of the performance evaluation. It is

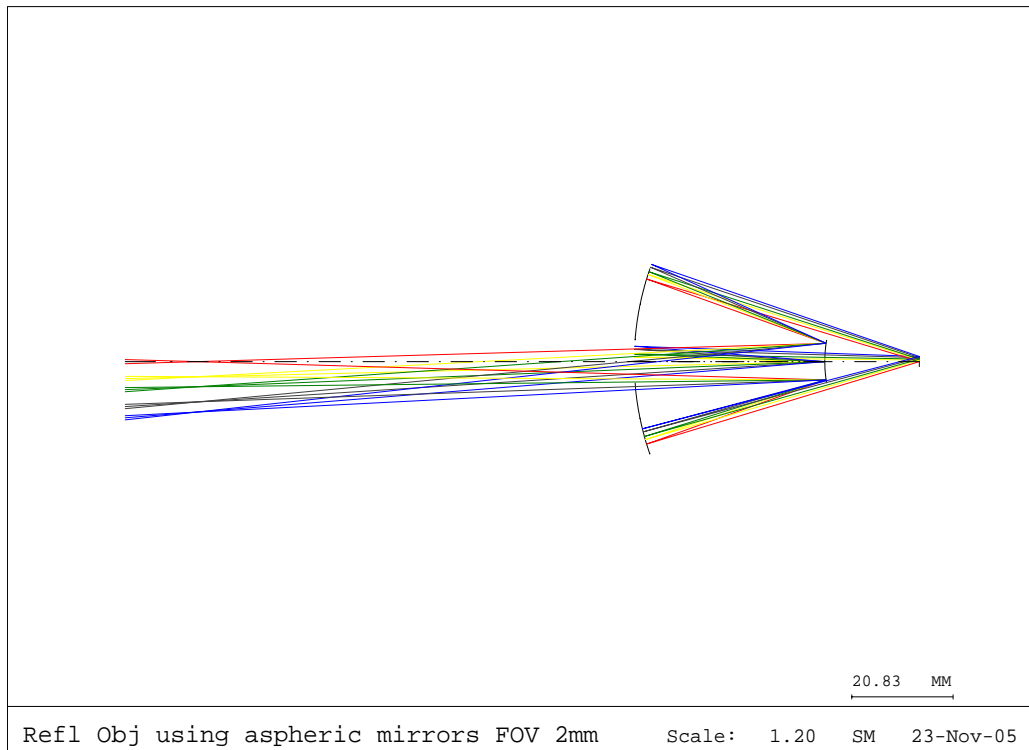


Figure 4.3: Layout of the final system design with aspheric mirrors

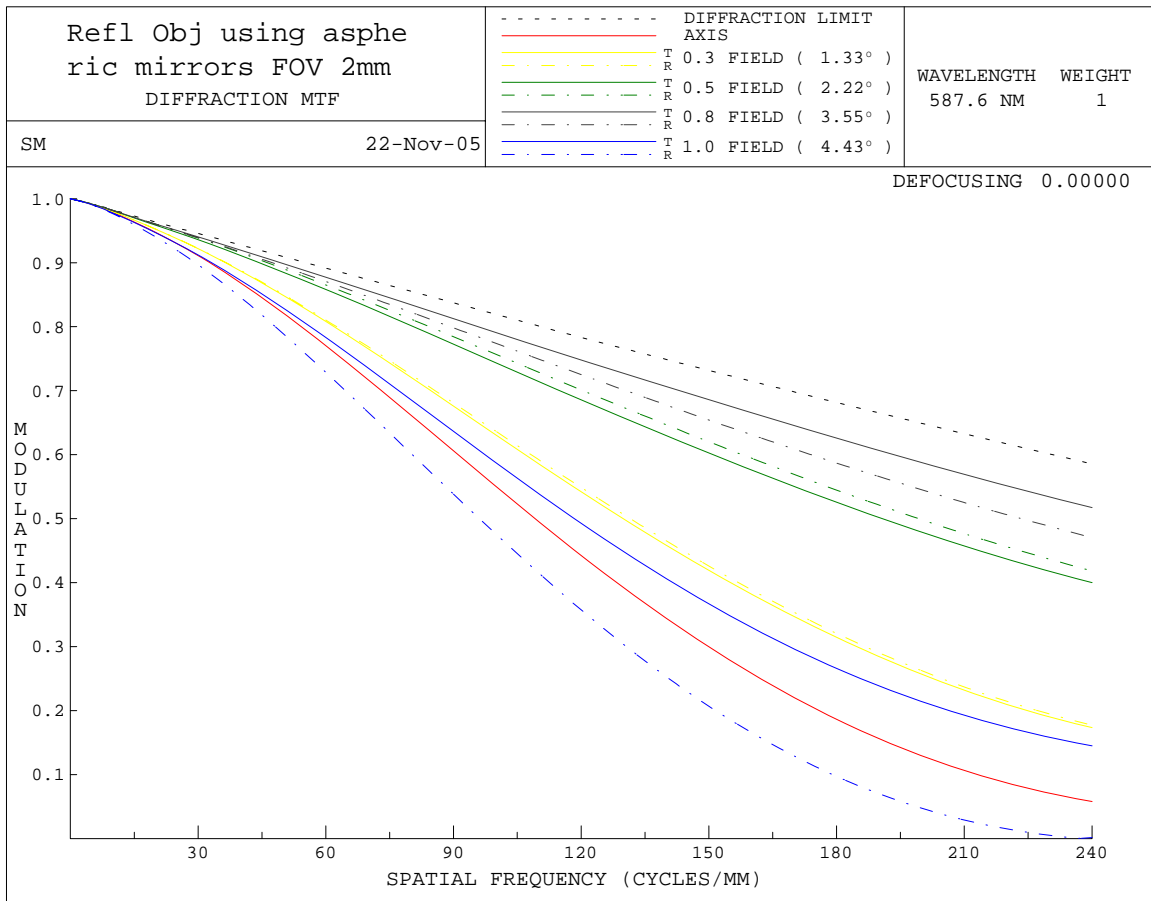


Figure 4.4: MTF plot for the reflecting microscope objective

evident that except for field curvature, the aberrations are negligible. The MTF holds well across smaller fields of view, however, it falls well below our target of 20% at the cut-off frequency of 250 lp/mm for the largest FOV namely 1mm. Also, because of the presence of the obscuration, the on-axis image contrast is lower than 20%. It can be observed from the astigmatic field curves that while astigmatism is minimal, the field curvature is significant and largely contributes to the drop in MTF. Therefore, the final design for a 2mm FOV has been optimized to just meet specifications of less than  $5\mu\text{m}$  resolution with a 10X magnification.

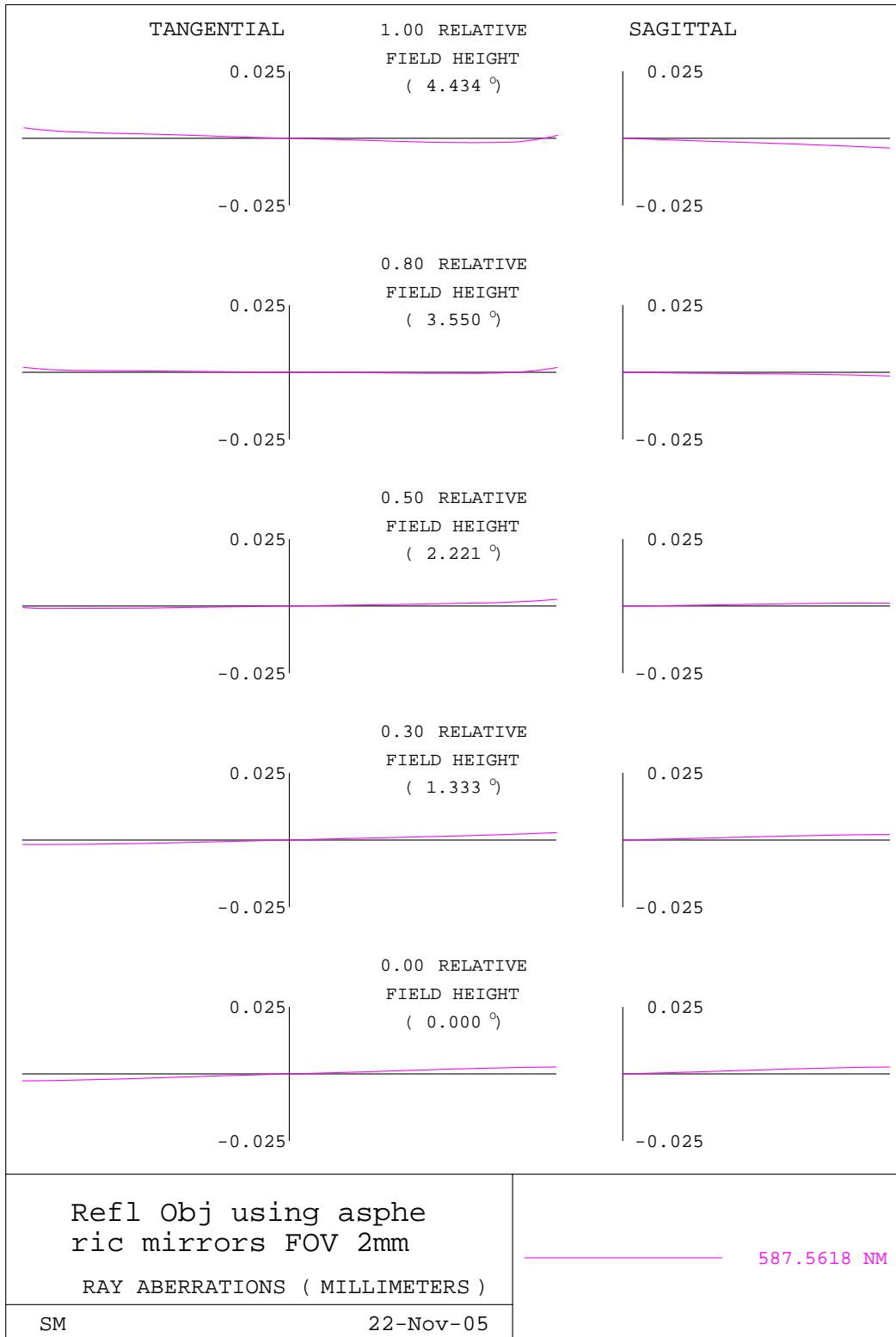


Figure 4.5: Ray aberration plot.

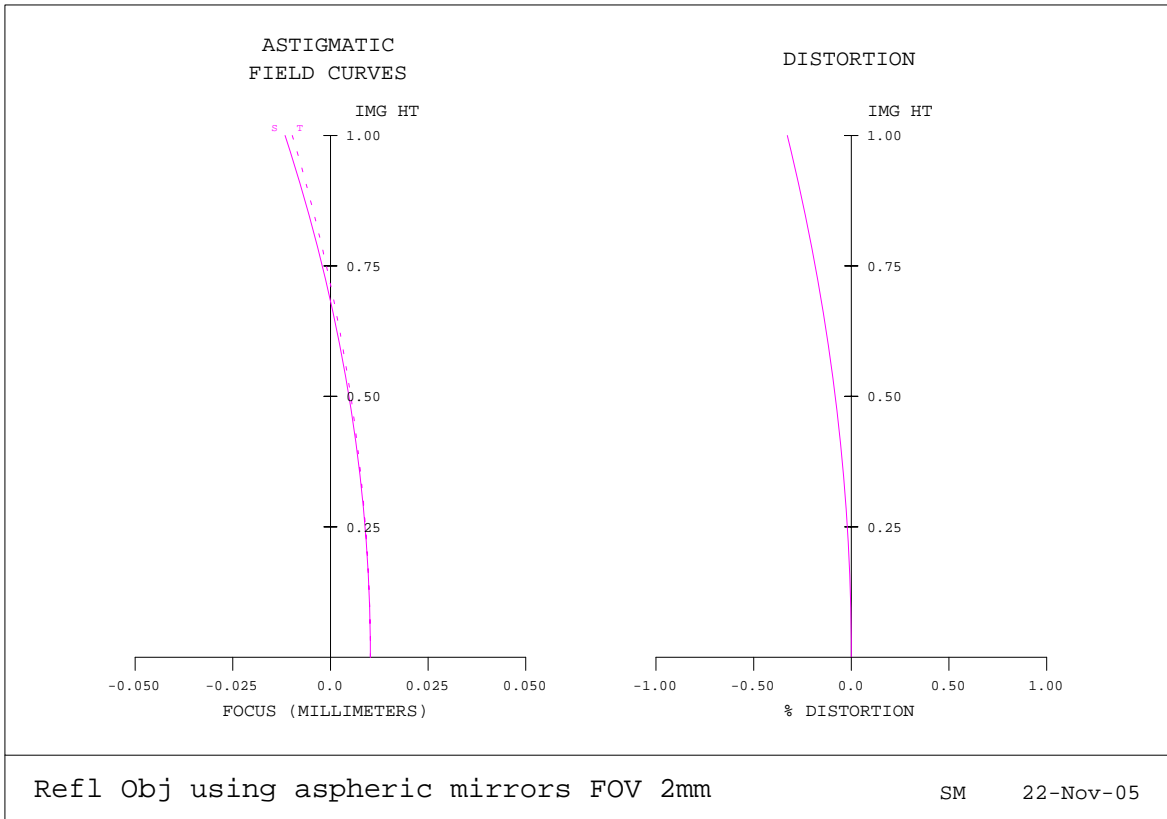


Figure 4.6: Astigmatism and distortion

The system has the several advantages. It has no refracting elements, nor optical cement, and no chromatic aberrations. This design also offers longer working distances, larger numerical apertures and greater useful bandwidth than conventional microscope objectives.

Such a design also has a few disadvantages. It is considerably larger diameter than a conventional refracting objective. However the primary drawback of the reflecting microscope objective is the large obscuration ratio for high NA systems. The obscuration in this design blocks about 30% of the light coming through, and therefore it needs a high intensity light source for performance comparable to an unobscured objective. Additionally, the obscuration modifies the Airy disc pattern by making the central spot smaller and the outer rings slightly brighter.



Moreover, the contrast ratio of the system collapses at the largest FOV of 2mm. During further analysis, a system with a FOV of 1.2 mm was observed to have a much more uniform MTF function of over 35% across all fields of view. Another significant problem that will arise in non-contact imaging such as the reflecting geometry discussed above is the large amount of spherical aberration and other aberrations that occur due to refraction in the tissue layers. The issue of accounting for biological samples in a converging beam was investigated by Westphal *et al.* (2002) where an approach for refraction correction in layered media through numerical correction using Fermat's principle was suggested [44]. These issues led to the investigation of an immersion refracting objective that offers uniform performance over larger FOV, and presents a solution for refraction effects at the tissue layers.

#### **4.2 Refracting Immersion Microscope Objective**

The resolution of the image through a microscope is limited by diffraction. The Raleigh criterion states that for a wavelength  $\lambda$  the smallest distance,  $d_{\min}$ , resolvable between two point sources as deduced from diffraction theory is

$$d_{\min} = 1.22 \times \frac{\lambda}{2NA} \quad 4.1$$

where the numerical aperture of the objective lens,  $NA$  equals  $n \sin \alpha$ ,  $n$  is the index of refraction in the object space, and  $\alpha$  is half the maximal angle under which the objective collects light from the object being imaged.

The numerical aperture of an objective may benefit from being large for two different reasons. Firstly, the spatial resolution increases with larger NA. Secondly, the collection efficiency, i.e.

the brightness of the image, increases rapidly with NA. The collection efficiency, measured in terms of the fraction of light collected from an isotropic light source is given by

$$\frac{\Omega}{4\pi} = \frac{1}{2}(1 - \cos \alpha) = \frac{1}{2} \left\{ 1 - \sqrt{1 - \left(\frac{NA}{n}\right)^2} \right\} \quad 4.2$$

where  $\Omega$  represents the solid angle of the cone of light. The solid angle versus numerical aperture is plotted in Fig. 4.6. It can be seen that the relationship between  $\frac{\Omega}{4\pi}$  and  $\frac{NA}{n}$  change from linear to quadratic and even faster for higher values of NA.

The refractive index of the imaging medium is critical in determining the working numerical aperture of a microscope objective. The numerical aperture is proportional to the refractive index

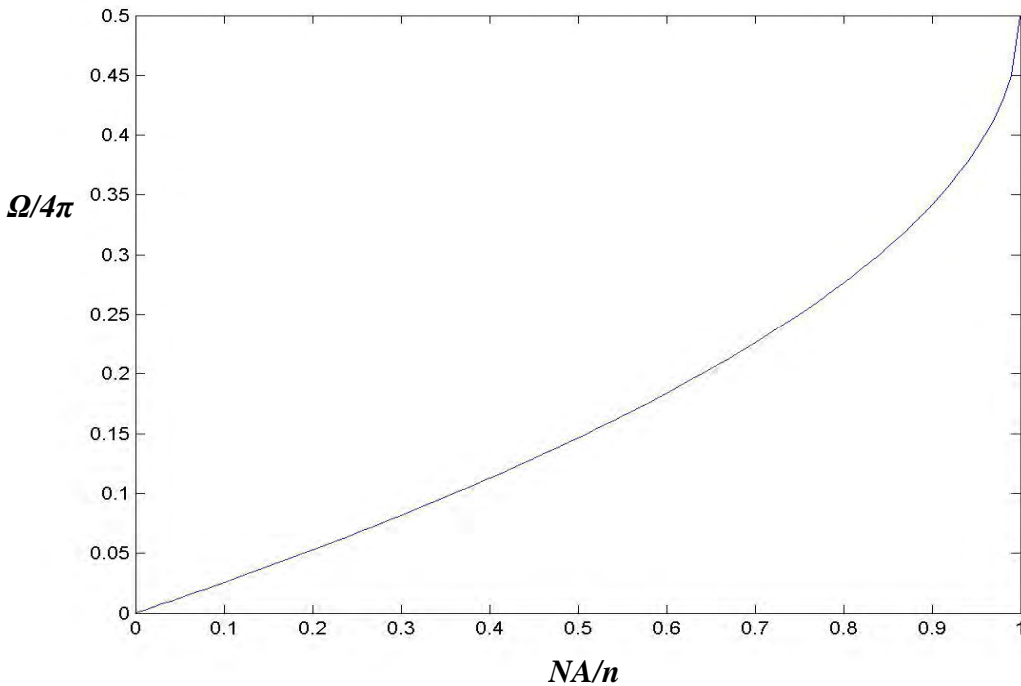


Figure 4.7: Variation of brightness with numerical aperture

of the imaging medium. Therefore, a dramatic increase in effective numerical aperture is observed when the objective is designed to operate with an immersion medium such as oil, glycerin, or water between the front lens and the specimen cover glass. Moreover, immersion oil contributes to two characteristics of the image viewed through the microscope: finer resolution and brightness than a conventional microscope. This is because of a small amount of defocus introduced by the refractive index mismatch between air and tissue and the air gap losses due to total internal reflection. These characteristics are most critical under high magnification, so the higher power, shorter focus objectives are usually designed for oil immersion.

Based on the first order layout of the probe, and the practical limitations due to manufacturing capabilities as explained and illustrated in Chapter 3, a 10X microscope objective was designed for a resolution of less than  $5\mu\text{m}$  (i.e.,  $4\mu\text{m}$ ) to meet the same specifications as the reflecting objective (see Table 4-2).

Table 4-2: Refractive objective - design specifications

<b>Object</b>	Size	2 mm
	Resolution	$\leq 5 \mu\text{m}$
	Depth	2 mm
<b>Microscope Objective</b>	Type	Refracting
	Numerical Aperture	0.28
	Magnification	10X
	Other Parameters	
	Wavelength	750-850 nm
	FOV	2 mm

#### 4.2.1 The starting point: An immersion refractive microscope objective without zoom

The first step in the design process was to model a 10X immersion refractive microscope objective with an NA of 0.28 while aiming for at least a  $10\mu\text{m}$  resolution performance. Such design would serve as a starting point for the final  $5\mu\text{m}$  or less resolution objective with dynamic focusing capability. Thus, from the  $10\mu\text{m}$  performance objective, the strategy was to incorporate additional components to allow for dynamic focusing and slowly converge the design to meet a target resolution of  $4\mu\text{m}$  required for our skin imaging application. Assuming a 10% drop in MTF caused by tolerances, we are looking to have at least 30% contrast across the spatial.

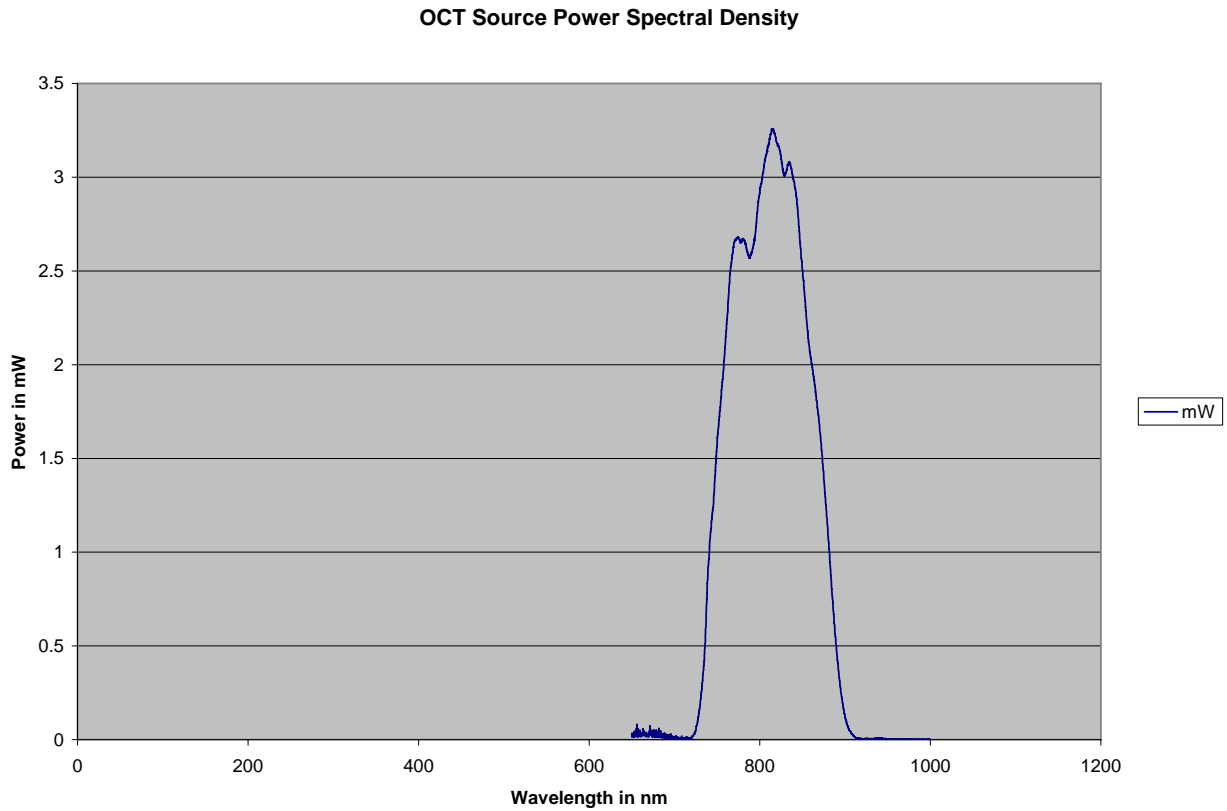


Figure 4.8: Source power spectrum used for system performance analysis.

So at an MTF spatial frequency of 100 cycles/mm (i.e. 1 cycle per 10 $\mu$ m or 100cycles/mm), our target was to achieve at least 30% contrast. The preliminary design was done using CodeV<sup>TM</sup> and the spectrum was weighted according to the source power spectrum centered at 800 nm illustrated in Fig.4.9.

Once a starting point was designed, the next step was to find an immersion oil/gel that has optimum transmission at 800 nm and closely matches the index of skin. The search led to a commercially available gel from the Cargille Labs, coded 0607. It has a refractive index of 1.46. There are no other known liquids, gels, or greases with significantly better transmittance at near IR. Each had wide temperature stability. Freezing points were below -67°C and boiling point exceeded 400°C. This means a more stable refractive index. Typical characteristics of the gel are shown in Appendix A.

A new material in the private glass catalog called 'MY GEL' was defined with all the index, dispersion and transmission properties as obtained from Cargille labs optical gel specifications. A new flat surface was incorporated along with a glass plate, and the system was further optimized for desired performance. After the desired resolution was obtained, glass was fitted lens by lens within the specified glass map boundaries (NFK5, NSK16, NLAF2, SF4). The following lens system was finalized with an excellent resolution of less than 5 $\mu$ m. The lens layout and MTF are shown in Fig. 4.9. The image of this system is diffraction limited, and the MTF at 250 cycles/mm is close to the diffraction limit.

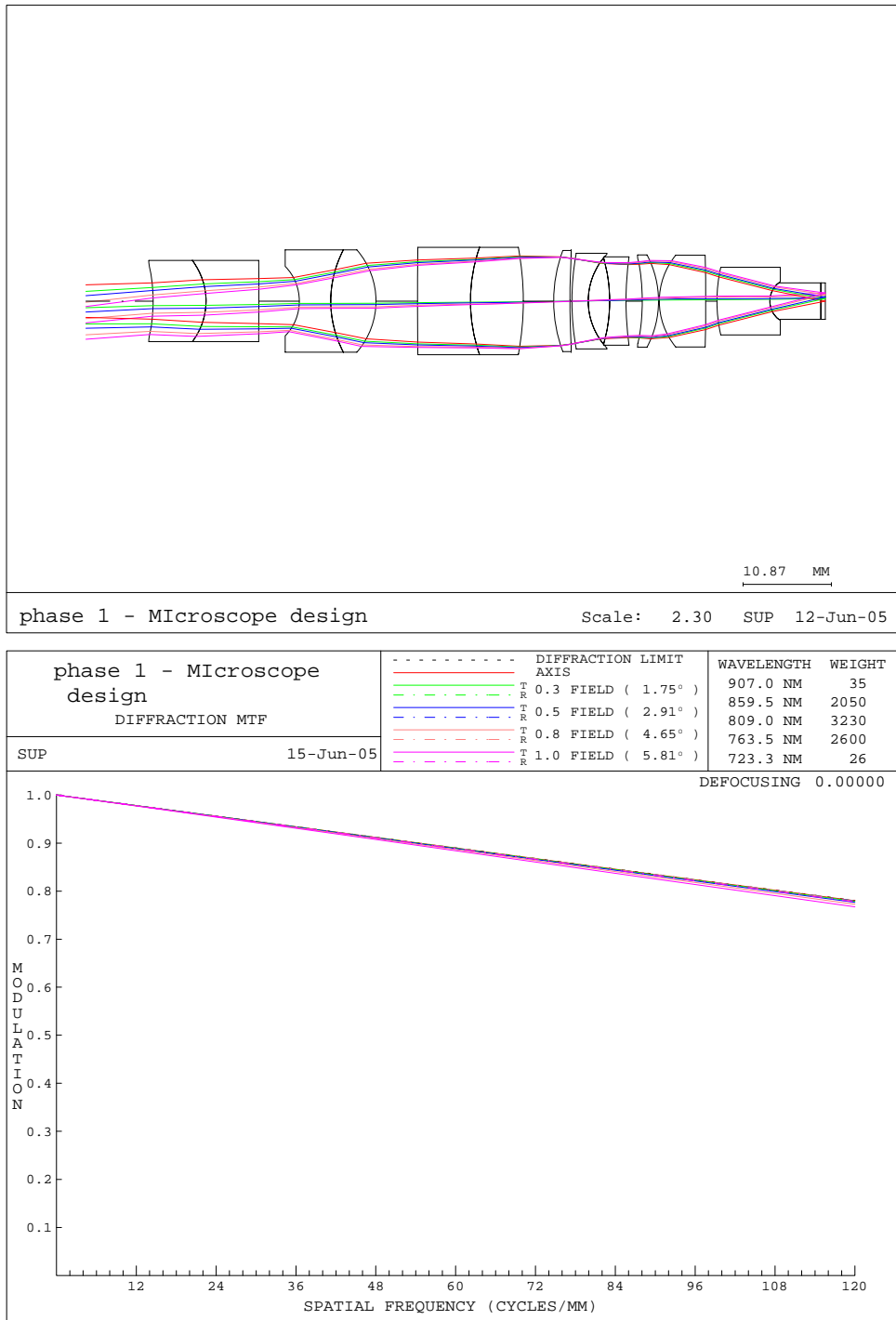


Figure 4.9: Preliminary design: lens layout (Top) and MTF (Bottom) at 100 cycles/mm

## 4.2.2 Simulating axial resolution – Zoom configuration and dynamic focusing element

We needed an imaging system that can image up to a skin depth of 2mm. So, the next step was the incorporate zoom positions in the system to be able to evaluate the image quality at different focus positions. Three zoom positions were added, at 0, 1 and 2mm depth of skin. A glass plate was added just before the immersion gel to represent a liquid crystal lens. At each zoom position the refractive index of the glass plate was set as an independent variable parameter. The radii of curvature of the two surfaces of the lens were set to vary similarly across all zoom positions. By optimizing the design, the ideal refractive indices of the three lenses that would focus at these depths were obtained ( $n=1.481$  at zoom=0mm;  $n=1.609$  at zoom=1mm;  $n=1.734$  at zoom=2mm). These were the starting parameters for the next step, which was to model a liquid crystal dynamic focusing element that will change its refractive index in order to refocus axially across 2mm.

### 4.2.2.1 Background – Liquid crystal

The liquid crystal refractive index may be varied as a function of position by adjusting the birefringence properties of the material. The birefringence is given by

$$\Delta n = n_e - n_o = \frac{r^2}{2df} \quad 4.3$$

where  $r$  is the radius of the lens,  $d$  is the cell gap,  $f$  is the focal length and  $\Delta n$  is the birefringence.

A liquid crystal can thus be modeled to function as a lens if the electric field is varied as a function of the radial distance from the center in order to approach the OPD of a lens of constant refractive index as demonstrated in Fig. 4.9. Thus, constant optical path difference can be maintained either by varying the curvature or the refractive index. In order to model such variations, we define a gradient index lens.

### 4.2.2.2 The Gradient Index lens

The GRIN profile in a lens element can be specified by a double power series which depends on the spatial coordinates in the element:

$$n(r, z) = n_{00} + n_{01}z + n_{02}z^2 + n_{03}z^3 + n_{04}z^4 + n_{10}r^2 + n_{20}r^4 + n_{30}r^6 + n_{40}r^8 \quad 4.4$$

where  $n$  is the index at some point in the lens,  $n_{00}$  is the base index of the lens,  $n_{0i}$  and  $n_{0j}$  are coefficients of the index gradient and  $r$  is the radial position where the index is evaluated ( $r^2 = x^2 + y^2$ ). When the index of refraction depends only on the distance from the optical axis  $r$ , the gradient is said to be radial. Its representation simplifies Equation 4.4 as

$$N(r) = N_{00} + N_{10}r^2 + N_{20}r^4 + \dots \quad 4.5$$

The coefficients of the radial index gradient contribute in several ways to the design.  $N_{00}$  is the index of the base glass, which is the index specified in a homogeneous design.  $N_{10}$  contributes to the power of a thin Wood lens and to the Petzval field curvature due to the gradient.  $N_{20}$  has no effect on the Petzval curvature, and can thus be used to correct other aberrations without affecting the Petzval curvature.

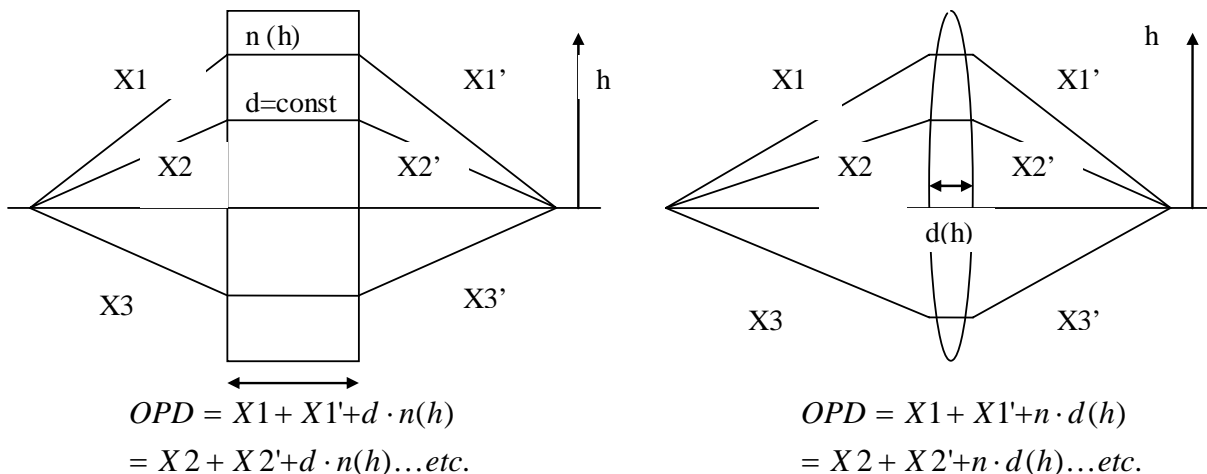


Figure 4.10: Defining a Wood lens (Gradient index lens with a radial index gradient)



A gradient index lens, or a Wood lens [46], was substituted in place of the initial lens of homogeneous refractive index. A gradient index lens in CodeV<sup>TM</sup> may be specified as a lens with a custom glass property i.e., it is defined as a private glass catalog with a base index at different wavelengths and radial coefficients as defined above. Note that the radial coefficients and base index have alone been defined as variable parameters for optimization of the gradient lens. This simulates what is known as a Wood lens, which is a flat glass plate as introduced in Section 4.2.2.1 above. The radial coefficients were coupled to vary simultaneously over all zoom positions, while the base index was optimized independently over each zoom position.

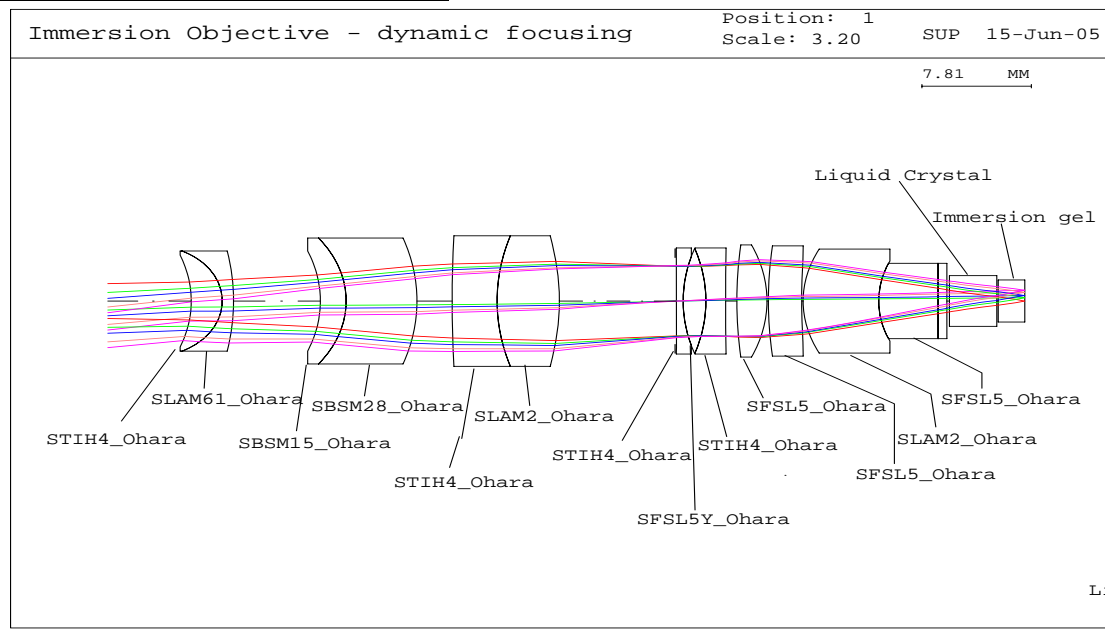
Simulation and optimization of the liquid crystal led to a resolution of less than 5  $\mu\text{m}$ . With more time for optimization, the resolution can be improved even further. The lens layout, first-order data, and the MTF plots are given as a function of the zoom position in Fig. 4.10 and Fig. 4.11 and Table 4-3 (all units are in mm). MTF falls well above 20% for the required spatial frequency of 250 cycles/mm, thus giving a resolution of 4 $\mu\text{m}$ .

This system has one primary limitation, the speed of the LC lens. Scanning the 2mm $\times$ 2mm sample at video rate (30 frames/sec) requires a depth scan approximately every 3 millisecond. Typically, a 6mm diameter LC lens can refocus in approximately 1 second. In our design, we require an LC of approximately 3mm diameter, and the time estimate for dynamically refocusing this lens would be 0.5 seconds, which is still orders of magnitude slower than necessary for imaging at video rate.

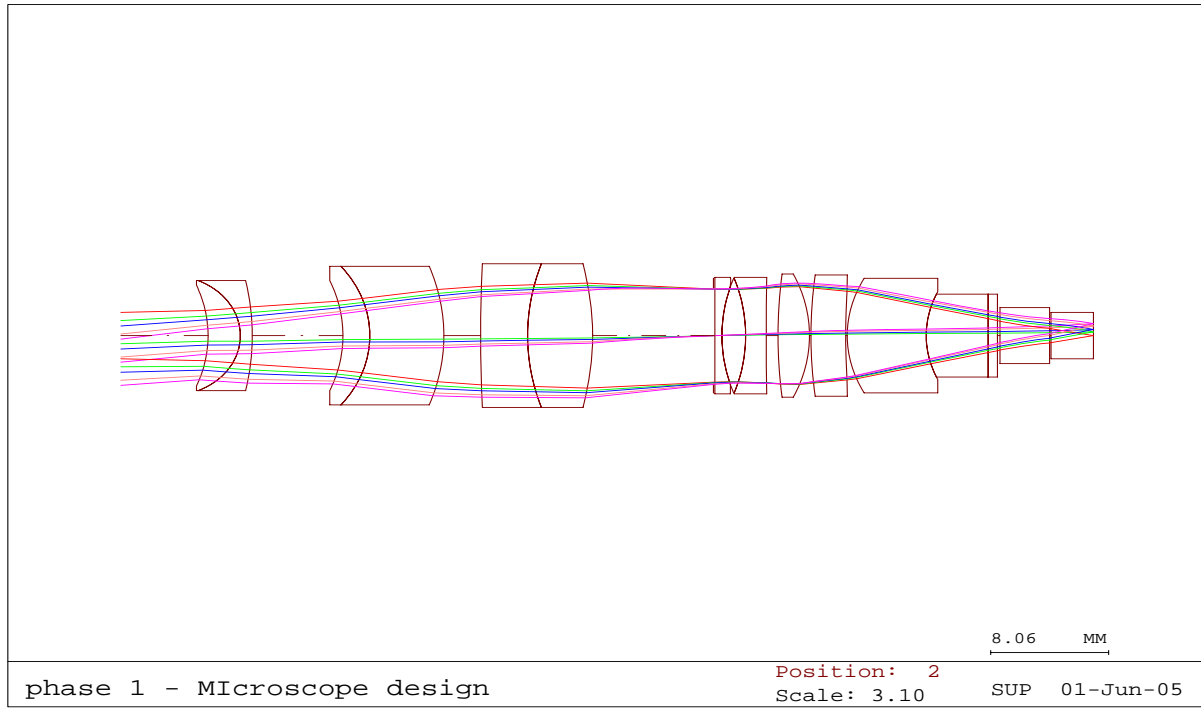
Table 4-3: First order parameters of the system.

INFINITE CONJUGATES		POS1	POS2	POS3
	EFL	10.1255	11.6360	11.9210
	BFL	1.0767	1.7348	2.6759
	FFL	10.6111	6.6853	6.6122
	FNO	1.7318	1.6508	1.6493
AT USED CONJUGATES	RED	0.0830	0.1000	0.1025
	FNO	1.7857	1.7857	1.7857
	OBJ DIS	73.4851	73.4851	73.4851
	TT	133.0066	134.0066	135.0066
	IMG DIS	1.8902	2.8902	3.8902
	OAL	57.6312	57.6312	57.6312
PARAXIAL IMAGE	HT	1.0000	1.0000	1.0000
	THI	1.9166	2.8984	3.8983
	ANG	7.9579	6.6043	6.4408
ENTRANCE PUPIL	DIA	4.0282	4.8563	4.9799
	THI	13.2039	13.2039	13.2039
EXIT PUPIL	DIA	10.8380	5.9725	6.2048
	THI	26.1667	12.5755	12.1773
	STO DIA	6.2727	7.6148	7.8181

**ZOOM 1 – 0 mm focus in skin surface**



**ZOOM 2: 1 mm focusing in the skin**



**ZOOM 3 – 2 mm focusing in the skin**

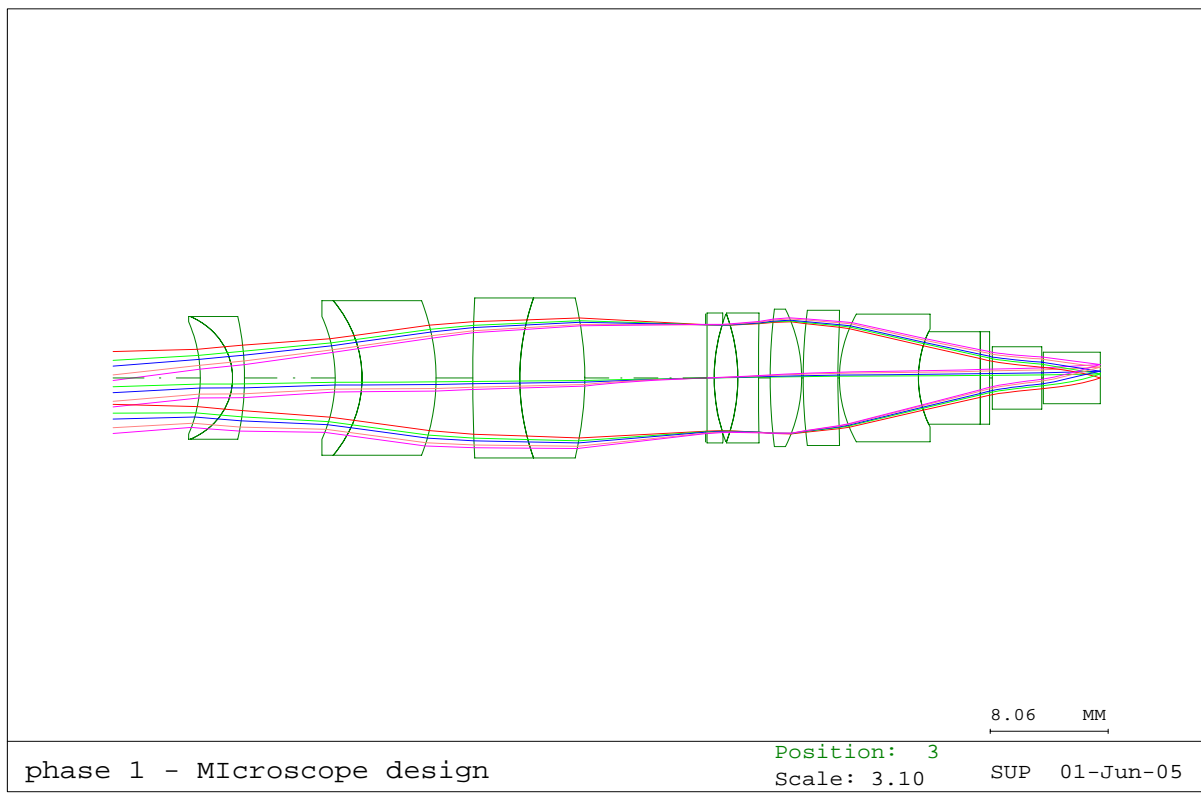
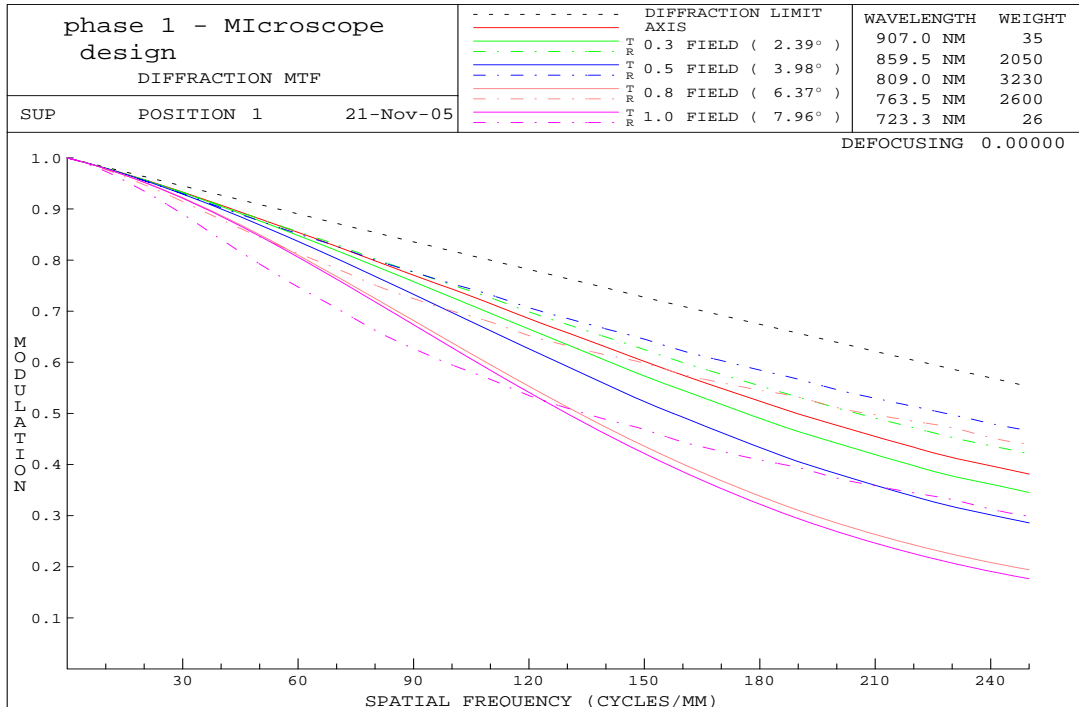
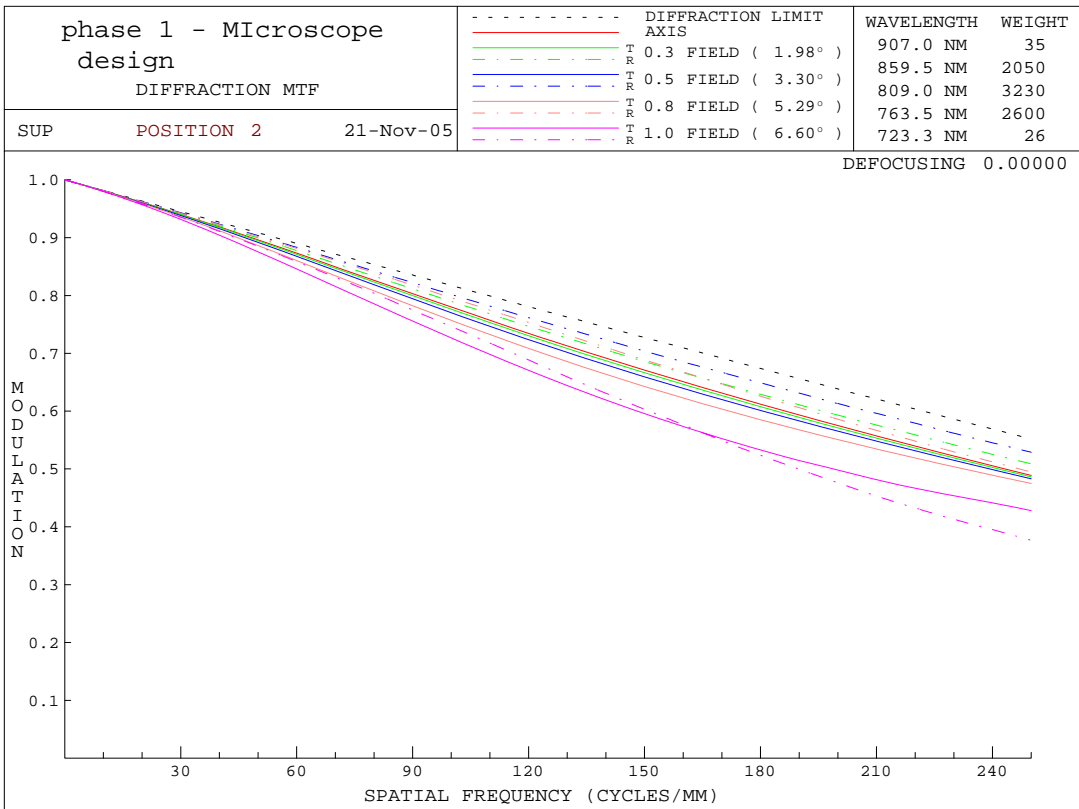


Figure 4.11: Lens layout of final design in zoom positions 1, 2 and 3.

## ZOOM 1



## ZOOM 2



### ZOOM 3

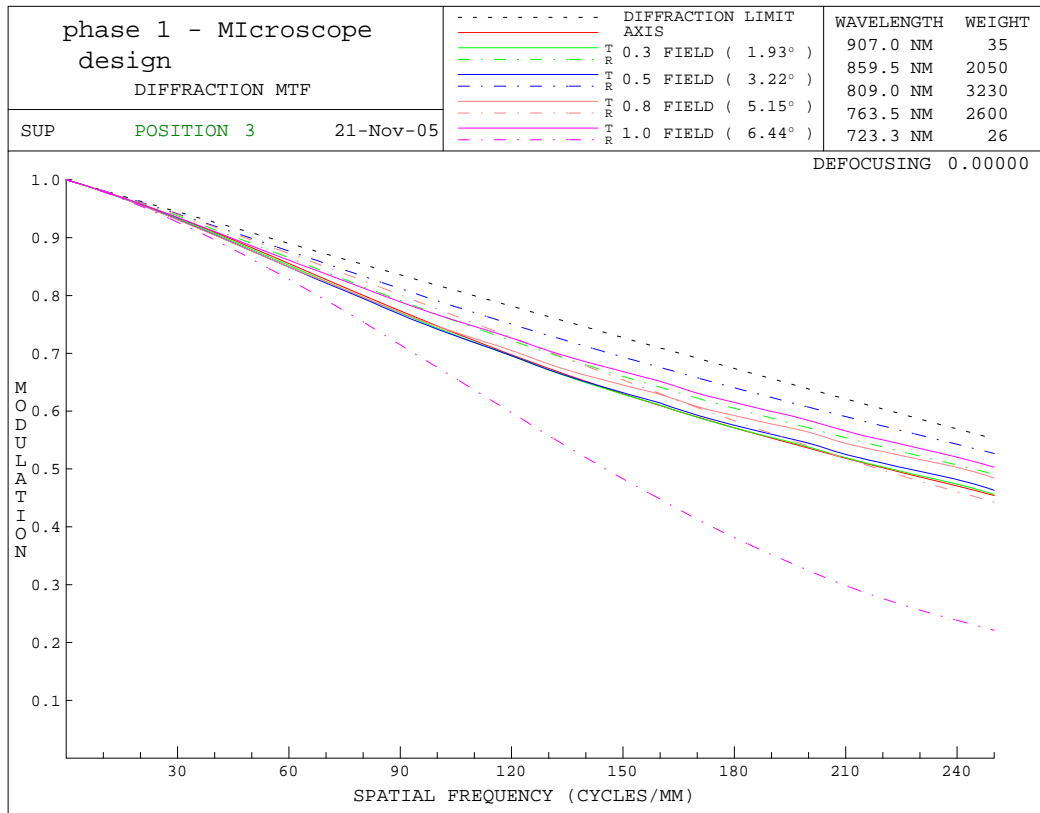


Figure 4.12: MTF at the three zoom positions.

#### 4.2.3 Tolerancing the System

Determining the sensitivity of a system to fabrication errors is a crucial step in an optical system design process. Therefore, designing a robust system that is pre-evaluated for its tolerance to manufacturing inaccuracies is a critical link between design and engineering. A thorough tolerance assignment contributes significantly towards the improvement of the production cost factor, process selection, tooling, set-up cost, required operator skills, inspection, and scrap and rework. System tolerances that are too tight can limit the choice in optical fabrications shops available that can meet the demand for very high accuracy. Importantly, tight tolerances increase the fabrication, assembly and testing costs.

Therefore, a rational and exhaustive algorithm is necessary to predict the tolerances of a system. Statistical methods are a powerful tool that can assess the effect of deviations on system performance. Moreover, such predictive algorithms can be used to devise compensation parameters to simulate adjustments that can be made during the assembly process.

Table 4-4: Tolerance limits for different cost categories-adapted from K.P Thompson and L.Hoyle, 1994 [47].

	<b>Catalog</b>	<b>Regular</b>	<b>Select</b>	<b>Premium</b>	<b>Ultimate</b>
<b>Index</b>	0.001	0.0005	0.0003	0.0002	0.0001
<b>Homogeneity</b>	0.0001	0.00002	0.000005	0.000002	0.000001
<b>Radii</b>	5%	1%	0.50%	0.10%	0.05%
<b>C.T in mm</b>	0.2032	0.127	0.0508	0.0254	0.00635
<b>Irreg. (fringes)</b>	2 – 1/4	2 – 1/4	1/4 -1/8	1/8-1/20	1/50
<b>Wedge in rad</b>	0.001454	0.000291	0.0009691	0.000242	4.85E-05
<b>Tilt in rad</b>	0.001454	0.000291	0.0009691	0.000242	4.85E-05
<b>Decenter in mm</b>	0.1016	0.0508	0.0254	0.00635	0.00254
<b>TIR in mm</b>	n/a	0.0127	0.0127	0.00635	0.00254

A tolerance analysis was conducted in CodeV™ for the refractive microscope objective using Optical Research Associates' proprietary wavefront differential algorithm for diffraction MTF performance measures. In this algorithm, a single ray trace of the nominal system is used to compute the differential wavefront changes as a function of the parameter changes, for each tolerance limit. The function is then extended into a function of multiple variables by taking permutations of wavefront differentials for two parameters at a time. These results are then statistically combined to arrive at an overall system performance prediction, along with the individual MTF performance values for

each surface. The tolerance analysis was executed in the inverse sensitivity mode, where tolerance values are varied within user-defined limits and each limit is optimized to have approximately the same impact on the system performance. The variation limits were defined based on Table 4-4, taking into account the incurring manufacturing costs. The tolerance limits were set to fall within the ‘Select’ cost category (See Table 4-5). A system tolerance was also specifically executed for the radial index gradient element. Displacement compensators were set for the sub-system after the aperture stop, and a thickness compensator was included for the image surface defocus. A macro file, adapted from an original file provided by Jeff Hoffman of Optical Research Associates, was generated for the microscope lens based on the above tolerances specification.

Table 4-5: Defined tolerance limits –Select cost category

<b>Tolerance limits</b>	<b>MINIMUM</b>	<b>MAXIMUM</b>
<b>Radius</b>	0.5%	
<b>Irregularity</b>	0.25	1
<b>Thickness</b>	0.05	0.1
<b>Index</b>	0.0003	
<b>Inhomogeneity</b>	0.000005	0.00002
<b>TIR</b>	0.01	0.1
<b>Tilt</b>	0.001	0.1
<b>Decenter</b>	0.025	0.1
<b>Roll</b>	0.025	0.1

In the final evaluation, the overall system performance showed a drop of approximately 15% in diffraction MTF. Individual surfaces demonstrated an MTF drop of less than 2% because of parameter variations. There were a few exceptions at high field of view for surfaces with large curvature. However, the drop in MTF in these cases did not exceed 2.5%. Ideally we would want to constrain up to a 10% drop in MTF in order to allow room for further improvement in resolution down to 2 $\mu$ m. Further optimization of the

parameters can enable higher resolution and lower sensitivity of the parameters. The system tolerances for centered and decentered tolerances and the performance summary for the three zoom configurations are shown in appendix A.



## CHAPTER 5 - CONCLUSION AND FUTURE WORK

Optical Coherence Tomography (OCT) is a non-invasive optical imaging and diagnostic technique that has come into practice in the last few decades because of its accurate, high resolution images over three-dimensional cross-sections of biological tissue. The first commercial application of OCT was in ophthalmology because of the very high penetration achieved in transparent tissue. Thereafter, its relevance in other medical imaging applications was investigated and dermatology emerged as one of the most promising areas that could fully exploit the advantages of OCT. Imaging the epithelium at depths of up to 3mm has been achieved. However, maintaining high transverse resolution with high depth resolution remains a critical challenge. Dynamic focusing for each axial scan of the tissue provides an effective solution for quasi-invariant resolution throughout the depth of sample.

Different implementations of dynamic focusing have been reviewed in previous literature. In this thesis, we have proposed a theoretical model for a dynamic focusing OCT imaging probe developed in the paraxial regime for high-resolution performance in the near infra-red spectrum. This model incorporates dynamic focusing in two configurations. The first involves a reflecting microscope objective and requires a few moving parts. The second involves a refracting microscope objective and requires no moving parts.

The design, modeling, and analysis of the two microscope objectives and their primary limitations and advantages have been discussed in detail. Results show that for the design

specifications that include a relatively large FOV, the refractive design is significantly superior in performance to the reflective design. The incorporation of a dynamic focusing element, namely a liquid crystal lens within the refracting microscope objective was successfully modeled using a gradient index lens and the system has been analyzed for performance and sensitivity to fabrication errors. The main drawback of the refractive system that makes it unsuitable for *in vivo* imaging of tissue is that the liquid crystal technology presently available for the given system specifications limits the speed of scan. Scanning a 2mm×2mm sample at video rate (30 frames/sec) necessitates a z-scan to be completed every 3.3 milliseconds in order to ensure maximum efficiency. However, scanning speed is reduced to the order of hundreds of milliseconds for a liquid crystal lens between 1 and 3 mm in diameter. Future work will involve the development of innovative methods to improve scanning speed or to come up with other implementations of the gradient index variable focus lens to make the instrument commercially viable. Also, the other, more conventional, components of the probe will be designed and the imaging probe will be assembled and tested in an interferometric OCT setup.

Dynamic focusing is a crucial capability for invariant high resolution OCT imaging of non-transparent tissue samples and this work provides a path toward the development of novel probes that provide a working solution that incorporates the capability.

## APPENDIX A

### CARGILLE LABS IMMERSION GEL 0607 -TYPICAL CHARACTERISTICS

**CARGILLE**  
**OPTICAL GEL CODE 0607**  
 $n(5893 \text{ \AA})_{25^\circ\text{C}} = 1.457$   
**TYPICAL CHARACTERISTICS**

May 15, 2004

<u>COMPOSITION</u> .....	Aliphatic Hydrocarbons & Gelling Agents
<u>APPEARANCE</u> .....	Colorless to Slightly Yellow Gel
<u>ODOR</u> .....	None
<u>COLOR STABILITY</u> .....	In sun: may slightly yellow after 9 years
<u>INDEX CHANGE RATE BY EVAPORATION</u> .....	Very low: 0.0000 expected:
exposed surface area to volume ratio of 0.2 sq. cm / cc @ 25 °C for 32 days	
<u>FREEZING POINT</u> °C.....	-67
<u>BOILING POINT</u> °C @ 760mm Hg.....	> 416
<u>FLASH POINT</u> °C COC.....	> 245
<u>DENSITY</u> g/cc @ 25 °C.....	0.848
<u>DENSITY TEMP. COEF.</u> g/cc / °C.....	-0.0006
<u>COEF. OF THERM EXP.</u> cc/cc / °C.....	0.0007
<u>VISCOSITY</u> @ 25 °C.....	Soft Gel
<u>OIL SEPARATION</u> 100 °C for 24 Hours, % by Weight .....	< 0.05
<u>WEIGHT LOSS</u> 100 °C for 24 Hours, % .....	< 0.05
<u>WATER IMMERSION</u> .....	Gel disperses
<u>PARTLY SOLUBLE:</u> Carbon Tetrachloride, Ethyl Ether, Freon TF, Heptane, Methylene Chloride, Naphtha, Toluene, Turpentine, Xylene	
<u>INSOLUBLE:</u> Acetone, Ethanol, Water	<u>CLEANUP:</u> Wipe surfaces clean, then use soap and water.
<u>COMPATIBLE</u> 10 month immersion @ 25 °C: Acrylic, Cellulose Acetate, Epoxy, Mylar, Nylon, Polycarbonate, Polyester, Polyethylene, Polypropylene, Polystyrene, Polyurethane, Polyvinyl Chloride, Phenolic, Teflon; Silicone, and Fluorosilicone Rubber; Neoprene Rubber, Aluminum, Copper, Brass, and Steel; ( tests done on one example of each )	
<u>INCOMPATIBLE:</u> Latex Rubber, Tygon ( types: S-50-HL, R-3603, B-44-3 )	
<u>TOXICITY</u> .....	Low ( request MSDS )

CAUCHY EQUATION: refractive index as a function of wavelength at 25 °C

W = wavelength in angstroms ( Å )

$$n(W) = 1.44503 + (440960) / W^2 + (-2.85878E+11) / W^4$$

SOURCE OR SPECTRAL LINE	WAVELENGTH ( angstroms )	REFRACTIVE INDEX 25 °C	% TRANSMITTANCE 25 °C		
			1mm	1 cm	10cm
near UV cut off	3200	1.485	83	15	0
i ( Hg )	3650	1.477	98	81	12
h ( Hg )	4047	1.471	99	92	42
F? ( Cd )	4800	1.464	100	98	78
F ( H )	4861	1.463	100	98	79
e ( Hg )	5461	1.459	100	99	86
D ( Na: D1, D2 mean )	5893	1.457	100	99	90
HeNe laser	6328	1.456	100	99	92
C? ( Cd )	6439	1.456	100	99	90
C ( H )	6563	1.455	100	99	92
Ruby Laser	6943	1.454	100	100	98
GaAs laser	8400	1.451	100	100	99
Nd YAG laser	10648	1.449	100	95	61
Diode	13000	1.448	99	91	39
Diode	15500	1.447	98	80	11
$n_F - n_C$	=	0.008			
Abbe $v_D : (n_D - 1) / (n_F - n_C)$	=	57			
Temp. Coef: $dn_D / dt$ 15-35 °C	=	-0.00035			

**CARGILLE LABORATORIES, INC.**

55 Commerce Road, Cedar Grove, NJ 07009-1289 U.S.A.  
 Phone: 973-239-6633 / Fax: 973-239-6096 / URL : www.cargille.com

## APPENDIX B

### TOLERANCES AND PERFORMANCE SUMMARY

07-Nov-05

POSITION 1

CENTERED  
TOLERANCES

phase 1 - Microscope design

SUR	RADIUS	RADIUS TOL	FRINGES POW/IRR	THICKNESS	THICKNESS TOL	GLASS	INDEX TOL	V-NO (%)	INHOMOGENEITY
0				73.48514	0.07500				
1	-11.12553	0.0556	1.0/ 0.50	2.21356	0.07500	STIH4	0.00030		0.0000050
2	-4.95521	0.0248	4.0/ 1.00	0.80848	0.07500	SLAM61	0.00030		0.0000050
3	-22.54277	0.1127	4.0/ 1.00	6.19834	0.10000	AIR			
4	-11.66097	0.0583	2.0/ 1.00	1.84057	0.05000	SBSM15	0.00030		0.0000050
5	-9.09909	0.0455	4.0/ 1.00	5.06938	0.05000	SBSM28	0.00030		0.0000050
6	-16.41860	0.0821	3.0/ 0.75	2.50828	0.10000	AIR			
7	137.71104	0.6886	2.0/ 0.50	3.21088	0.10000	STIH4	0.00030		0.0000050
8	18.69763	0.0935	4.0/ 1.00	4.44806	0.10000	SLAM2	0.00030		0.0000050
9	-24.09083	0.1205	2.0/ 0.50	8.25728	0.05000	AIR			
10				0.10000					
11	-1582.60173	7.9130	2.0/ 0.50	0.48000	0.05000	STIH4	0.00030		0.0000050
12	14.11285	0.0706	4.0/ 1.00	1.61978	0.05000	SFSLEY	0.00030		0.0000050
13	-14.50007	0.0725	4.0/ 1.00	1.41198	0.05000	STIH4	0.00030		0.0000050
14	341.81907	1.7091	2.0/ 0.50	0.79930	0.05000	AIR			
15	45.03859	0.2252	3.0/ 0.75	2.15244	0.05000	SFSLEY	0.00030		0.0000050
16	-12.03703	0.0602	2.0/ 0.75	0.10000	0.05000	AIR			
17	42.07294	0.2104	3.0/ 0.75	2.38105	0.07500	SFSLEY	0.00030		0.0000050
18	83.60452	0.4180	3.0/ 0.75	0.10000	0.05000	AIR			
19	10.03864	0.0502	2.0/ 0.50	5.39687	0.05000	SLAM2	0.00030		0.0000050
20	8.53235	0.0427	4.0/ 1.00	4.23908		SFSLEY			
21	INF			0.63014	0.05000	535.935	0.00030		0.0000050
22	INF			0.18235	0.05000				
23	INF			3.38341	0.10000	'my	0.00030		0.0000050
24	INF			0.10000	0.05000				
25	INF			1.89331		'MYGELL'			
26	INF			-0.00308		'MYGELL'			

Radius, radius tolerance, thickness and thickness tolerance are given in mm.

Fringes of power and irregularity are at 632.8 nm. over the clear aperture

Irregularity is defined as fringes of cylinder power in test plate fit

Inhomogeneity is the non-focusable radial variation of index.

This is a fraction of the glass catalog homogeneity limits.

For unselected and H1 glass, the average expected value is

well below the upper limits given in the catalog and is

further reduced by refocusing. A reasonable HOM value is

25% of the catalog limit. For H4 glass, the average

expected value is closer to the catalog upper limits.

Typical values:  $25 \times 10^{-6}$  for unselected glass to  $1 \times 10^{-6}$  for H4

TOLERANCE LIMITS

	MINIMUM	MAXIMUM
* RADIUS	0.0200	
* SAG	0.0020	0.0500
** POWER	1.0	4.0
IRREGULARITY	0.25	1.00
THICKNESS	0.05000	0.10000
INDEX	0.00010	0.00200
INHOMOGENEITY	0.000005	0.000020

\* Radius tolerance is determined by both radius and sag limits

\*\* Power tolerance is between 2 and 4 times the irregularity tolerance

07-Nov-05

POSITION 1

DECENTERED  
TOLERANCES

phase 1 - Microscope design

ELEMENT NO.	FRONT RADIUS	BACK RADIUS	ELEMENT TIR	WEDGE ARC MIN	ELEMENT TILT TIR	TILT ARC MIN	EL. TIR	DEC/ROLL(R) mm.
1	-11.12553	-4.95521	0.0125 *	5.9				
1- 2	-11.12553	-22.54277			0.0038	1.8	0.0076	0.0250
2	-4.95521	-22.54277	0.0125 *	5.8			0.0293	0.0250 (R)
3	-11.66097	-9.09909	0.1050 *	45.2				
3- 4	-11.66097	-16.41860			0.0076	3.3	0.0019	0.0250
4	-9.09909	-16.41860	0.1050 *	42.8			0.0038	0.0250 (R)

tolerance_output_fre150_refracting-obj.txt									
5	137.71104	18.69763	0.1050 °	35.2					
5- 6	137.71104	-24.09083			0.0029	1.0	0.0126	0.0250	
6	18.69763	-24.09083	0.1050 °	35.0			0.0221	0.0250 (R)	
7	-1582.60173	14.11285	0.0125 °	5.4			0.0143	0.0250 (R)	
7- 9	-1582.60173	341.81907			0.0024	1.0	0.0007	0.0250	
7-14	-1582.60173	INF					0.0000	0.0005	
8	14.11285	-14.50007	0.0125 °	5.4					
9	-14.50007	341.81907	0.0125 °	5.4			0.0150	0.0250 (R)	
10	45.03859	-12.03703	0.0200 °	8.0	0.0058	2.3	0.0231	0.0250	
11	42.07294	83.60452	0.0100 °	4.1	0.0415	17.2	0.0027	0.0250	
12	10.03864	8.53235	0.0075 °	4.5					
12-14	10.03864	INF			0.0120	10.7	0.0203	0.0250	
13	8.53235	INF	0.1075 °	89.5					
13-14	8.53235	INF					0.0113	0.0250 (R)	
14	INF	INF	0.1050 °	93.3					
15	INF	INF	0.0100 °	11.2	0.0016	1.8	0.0000	0.1000	

Radii are given in units of mm.

For wedge and tilt, TIR is a single indicator measurement taken at the smaller of the two clear apertures. For decenter and roll, TIR is a measurement of the induced wedge and is the maximum difference in readings between two indicators, one for each surface, with both surfaces measured at their respective clear apertures. The direction of measurement is parallel to the original optical axis of the element before the perturbation is applied. TIR is measured in mm.

Decenter or roll is measured perpendicular to the optical axis in mm.

\* Tolerances on both sides of the element were added to obtain the wedge

T O L E R A N C E L I M I T S

	MINIMUM	MAXIMUM
TIR	0.0050	0.1000
TILT	0.0000	0.1000
DECENTER	0.0250	0.1000
ROLL	0.0250	0.1000

Probability Distribution Functions

	2nd moment	4th moment
Scalar tolerances	0.3333	0.2000 (1-D Uniform)
Irregularity	0.5000	0.3333 (2-D Uniform)
Decenter tolerances	0.3435	0.1870 (2-D Gaussian, truncated at 0.1353)

Additional tolerances used:

TYPE	VALUE
RAG S23	sym 0.0001000
07-Nov-05	

POSITION 1

P E R F O R M A N C E S U M M A R Y  
POLYCHROMATIC MODULATION TRANSFER FUNCTION

phase 1 - Microscope design

WAVELENGTH	WEIGHT
907.0 NM	35
859.5 NM	2050
809.0 NM	3230
763.5 NM	2600
723.3 NM	26

RELATIVE FIELD	FREQ L/MM	AZIM DEG	WEIGHT	DESIGN	DESIGN + TOL *	COMPENSATOR RANGE (+/-) *	DSX S11..22	asy	DSY S11..22	asy	DLT S26	sym
0.00, 0.00	150.00	TAN	100.00	0.6074	0.4603	0.048704			0.048102		0.217308	
0.00, 0.30	150.00	TAN	1.00	0.5781	0.4332	0.048704			0.048102		0.217308	
0.00, 0.50	150.00	TAN	1.00	0.5260	0.3763	0.048704			0.048102		0.217308	
0.00, 0.80	150.00	TAN	1.00	0.4362	0.2591	0.048704			0.048102		0.217308	

Page 2

tolerance\_output\_fre150\_refracting-obj.txt  
 0.00, 1.00 150.00 TAN 1.00 0.4201 0.2062 0.048704 0.048102 0.217308

-----  
 \* The probable change and cumulative probability results are based on the assumption that the distribution of the MTF converges to a Gaussian form.  
 The compensator range is a mean plus 2 Sigma value.  
 Linear compensators are in units of millimeters.  
 Angular compensators are in radians.  
 07-Nov-05

POSITION 2

PERFORMANCE SUMMARY  
 POLYCHROMATIC MODULATION TRANSFER FUNCTION

phase 1 - Microscope design

-----  
 WAVELENGTH WEIGHT  
 907.0 NM 35  
 859.5 NM 2050  
 809.0 NM 3230  
 763.5 NM 2600  
 723.3 NM 26

-----

RELATIVE FIELD	FREQ L/MM	AZIM DEG	WEIGHT	DESIGN	DESIGN + TOL *	COMPENSATOR RANGE (+/-) *		DLT S26	sym	
						DSX S11..22	asy	DSY S11..22	asy	
0.00, 0.00	150.00	TAN	1.00	0.6714	0.5267	0.048704		0.048102		0.271032
0.00, 0.30	150.00	TAN	1.00	0.6643	0.5159	0.048704		0.048102		0.271032
0.00, 0.50	150.00	TAN	1.00	0.6575	0.4990	0.048704		0.048102		0.271032
0.00, 0.80	150.00	TAN	1.00	0.6424	0.4544	0.048704		0.048102		0.271032
0.00, 1.00	150.00	TAN	1.00	0.5952	0.3635	0.048704		0.048102		0.271032

-----

-----  
 \* The probable change and cumulative probability results are based on the assumption that the distribution of the MTF converges to a Gaussian form.  
 The compensator range is a mean plus 2 Sigma value.  
 Linear compensators are in units of millimeters.  
 Angular compensators are in radians.  
 07-Nov-05

POSITION 3

PERFORMANCE SUMMARY  
 POLYCHROMATIC MODULATION TRANSFER FUNCTION

phase 1 - Microscope design

-----  
 WAVELENGTH WEIGHT  
 907.0 NM 35  
 859.5 NM 2050  
 809.0 NM 3230  
 763.5 NM 2600  
 723.3 NM 26

-----

RELATIVE FIELD	FREQ L/MM	AZIM DEG	WEIGHT	DESIGN	DESIGN + TOL *	COMPENSATOR RANGE (+/-) *		DLT S26	sym	
						DSX S11..22	asy	DSY S11..22	asy	
0.00, 0.00	150.00	TAN	1.00	0.6285	0.4672	0.048704		0.048102		0.276998
0.00, 0.30	150.00	TAN	1.00	0.6260	0.4636	0.048704		0.048102		0.276998
0.00, 0.50	150.00	TAN	1.00	0.6261	0.4577	0.048704		0.048102		0.276998

-----

Page 3



tolerance_output_fre150_refracting-obj.txt									
0.00, 0.80	150.00	TAN	1.00	0.6410	0.4392	0.046704		0.046102	0.276998
0.00, 1.00	150.00	TAN	1.00	0.6641	0.4280	0.046704		0.046102	0.276998

-----

\* The probable change and cumulative probability results are based on the assumption that the distribution of the MTF converges to a Gaussian form

The compensator range is a mean plus 2 Sigma value.  
 Linear compensators are in units of millimeters.  
 Angular compensators are in radians.

Tolerance coefficients can be saved with the lens to speed up subsequent TOR executions. SAVE is recommended here.  
 WARNING - Coefficients will be reinitialized if the lens is changed.

## LIST OF REFERENCES

1. D. Huang, E.A. Swanson, C.P. Lin, J.S. Schuman, W.G. Stinson, W. Chang, M.R. Hee, T. Flotte, K. Gregory, C.A. Puliafito, and J.G. Fujimoto, "Optical coherence tomography," *Science*, vol. 254, 1178-1181, 1991.
2. K.Takada, I. Yokohama, K. Chida, and J. Noda, "New measurement system for fault location in optical waveguide devices based on an interferometric technique," *Appl. Opt.*, vol. 26, 1603-1606, 1987.
3. P A. Flournoy, R W. McClure and G. Wyntje, "White-Light Interferometric Thickness Gauge," *Appl. Opt.*, vol. 11, 1907-1915, 1972.
4. F.Xu *et al.* "Confocal enhanced optical coherence tomography for nondestructive evaluation of paints and coatings," *Opt. Lett.*, vol. 24, 1808-1810, 1999.
5. T. Li, A. Wang, K. Murphy, and R.Claus , "White-light scanning fiber Michelson interferometer for absolute position-distance measurement," *Opt. Lett.*, vol. 20, 785-787, 1995.
6. W. Drexler, U. Morgner, F.S. Kartner, C. Pitris, S.A. Boppart, X.D. Li, E.P. Ippen, and J.G. Fujimoto, "In vivo ultrahigh-resolution optical coherence tomography," *Opt. Lett.*, vol. 24, 1221-1223, 1999.
7. W. Drexler, "Ultra-high resolution optical coherence tomography," *J. Biomed. Opt.*, vol. 9, 47-74, 2004.
8. R.C. Youngquist, S. Car, and D.E.N. Davies, "Optical coherence domain reflectometry: A new optical evaluation technique," *Opt. Lett.*, vol. 12, 158-160, 1987.
9. J A. Izatt, M. D. Kulkarni, H-W Wang, K. Kobayashi, and M. V. Sivak, Jr., "Optical coherence tomography and microscopy in gastrointestinal tissues," *IEEE J. Select. Topics Quantum Electron.*, vol. 2, 1017-1028, 1996.
10. M. Sergeev *et al.*, "In vivo endoscopic OCT imaging of precancer and cancer states of human mucosa," *Opt. Exp.*, vol. 1, 432-440, 1997.
11. J. Welzel, "Optical Coherence Tomography in dermatology: a review," *Skin Research Tech.*, vol. 7, 1-9, 2001.
12. J.M. Schmitt, M. Yadlowsky, and R.F. Bonner, "Sub-surface imaging of living skin with optical coherence microscopy," *Dermatol.*, vol. 191, 93-98, 1995

13. N.D. Gladkova *et al.*, “*In vivo* optical coherence tomography imaging of human skin: norm and pathology,” *Skin Res. Tech.*, vol. 6, 6-16, 2000
14. G.J. Tearney, B.E. Bouma, S.A. Boppart, B.Golubovic, E.A. Swanson and J.G. Fujimoto, “Rapid acquisition of *in vivo* biological images by use of optical coherence tomography,” *Opt. Lett.*, vol. 21, 1408–1410, 1996
15. Ik-Kyung Jang *et al.*, “Visualization of Coronary Atherosclerotic Plaques in Patients using Optical Coherence Tomography: Comparison With Intravascular Ultrasound,” *JACC*, vol. 39, 604-609, 2002.
16. U. Gerckens *et al.*, “Optical Coherence Tomography (OCT): Potential of a new high-resolution intracoronary imaging technique,”*Herz*, vol. 28, 496-500, 2003.
17. B.W. Colston, U.S. Sathyam, L.B. DaSilva, M.J. Everett, P. Stroeve and L.L. Otis, “Dental OCT,” *Opt. Express.*, vol. 3, 230–238, 1998.
18. M.E.Brezinski and J.G. Fujimoto, “Optical coherence tomography: High-resolution imaging in nontransparent tissue,” *IEEE J. Select. Topics Quantum Electron.*, vol. 5, 185-1192, 1999.
19. M.E. Brezinski, G.J. Tearney, B.E. Bouma, J.A. Izatt, M.R. Hee, E.A Swanson, J.F. Southern, and J.G. Fujimoto, “Optical coherence tomography for optical biopsy: Properties and demonstration of vascular pathology,” *Circulation*, vol. 93, 1206-1213, 1996.
20. M.R. Hee, J.A. Izatt, E.A. Swanson *et al.*, “Optical coherence tomography of the human retina,” *Arch. Opthamol...*, vol. 113, 325-332, 1995
21. S.A. Boppart, B.E. Bouma, C.Pitris, J.F. Southern, M.E. Brezinski, and J.G. Fujimoto, “*In vivo* cellular optical coherence tomography imaging,” *Nature medicine*, vol. 4, 861-865, 1998.
22. E. Bordenave *et al.*, “Wide-field optical coherence tomography: imaging of biological tissues,” *Appl. Opt.*, vol. 41, 2059-2064, 2002.
23. J.G. Fujimoto, “Optical and Acoustical imaging for biological media- Optical Coherence Tomography,” *C. R. Acad. Sci Paris*, vol. 2, 1099-1111, 2001.
24. F.I. Feldschtein *et al.*, “*In vivo* OCT imaging of hard and soft tissue of the oral cavity,” *Opt. Exp.*, vol. 3, 239-250, 1998.
25. D. Spitzer and J. J. ten Bosch, “The absorption and scattering of light in bovine and human dental enamel,” *Calc. Tiss. Res.*, vol. 17, 129-137 (1975).

26. J. J. ten Bosch and J. R. Zijp, "Optical Properties of Dentin" in *Dentine and Dentine Reactions in the Oral Cavity*, A. Thylstrup, S. A. Leach, and V. Qvist, eds. (IRL Press Ltd., Oxford, 1987).
27. A.F.Fercher and E. Roth, "Ophthalmic laser interferometry," *Proc. SPIE*, vol. 658, 48–51, 1986
28. J.A. Izatt, "Optical coherence microscopy in scattering media," *Opt. Lett.*, vol. 19, 590–591, 1994.
29. C.A. Akcay, P. Parrein, and J.P. Rolland, "Estimation of longitudinal resolution in optical coherence imaging," *Applied Optics*, vol. 41, 1-7, 2002.
30. A.F. Fercher, W. Drexler, C.K. Hitzenberger, and T. Lasser, "Optical coherence tomography –principles and applications," *Rep. Prog. Physics*, vol. 66, 239-303, 2003.
31. A.F. Fercher, C.K. Hitzenberger, G. Kamp, and S.Y. El Zaiat, "Measurement of intraocular distances by backscattering spectral interferometry," *Opt. Comm.*, vol. 117, 43-48, 1995
32. G. Häusler and M.W. Lindner, "Coherence radar and spectral radar- New tools for dermatological diagnosis," *J. Biomed. Opt.*, vol. 3, 21-31, 1998
33. J.P. Rolland, and P. Delfyett, "Three dimensional optical imaging colposcopy," U.S. Patent 5, 921, 9 26, July 13, 1999.
34. J.P. Rolland, and P. Delfyett, "Three dimensional optical imaging colposcopy," U.S. Patent 6,141,577, Oct. 31, 2000
35. J.M. Schmitt, S.L. Lee, and K.M. Yung, "An optical coherence microscope with enhanced resolving power in thick tissue," *Optics Comm.*, vol. 142, 203-207, 1997.
36. B.M. Hoeling *et al.*, "An Optical coherence microscope for three dimensional imaging for developmental biology," *Opt. Exp.*, vol. 7, 136-146, 2000.
37. F. Lexer *et al.*, "Dynamic coherent focus OCT with depth independent transversal resolution," *J. Mod. Opt.*, vol. 46, 541-553, 1999.
38. B. Qi, A.P. Himmer, L.M. Gordon, X.D. Yang, L.D. Dickensheets, I.A. Vitkin, "Dynamic focus control in high-speed optical coherence tomography based on a microelectromechanical mirror," *Optics Comm.*, vol. 232, 123-128, 2004.
39. Divetia *et al.*, "Dynamically focused optical coherence tomography for endoscopic applications," *Appl. Phys. Lett.*, vol. 86, 103902, 2005.

40. J.G. Fujimoto, B. Bouma, G.J. Tearney, S.A. Boppart, C. Pitris, J.F. Southern, and M.E. Brezinski, "New technology for high speed and high resolution optical coherence tomography," *Ann. NY Acad. Sci.*, vol. 838, 95-107, 1998
41. Dubois, K. Grieve, G. Moneron, R. Lecaque, L. Vabre, C. Boccara, "Ultra-high-resolution full-field optical coherence tomography," *App. Opt.*, vol. 43, 2874-2883, 2004.
42. C.R. Burch, "Reflecting Microscopes", *Proc. Phys. Soc*, vol. 59, 41-46, 1946.
43. R. Kingslake, *Optical System Design*, 1<sup>st</sup> ed. London : Academic Press Inc., 1983
44. V. Westphal, A.M. Rollins, S. Radhakrishnan, and J.A. Izatt, "Correction of geometric and refractive image distortions in optical coherence tomography applying Fermat's principle," *Opt. Exp.*, vol. 10, 397-404, 2002
45. Klaus D. Mielenz, "Spherically Corrected Reflecting Objective for Unit Magnification," *Appl. Opt.*, vol. 13, 2580-2584, 1974.
46. L.G. Atkinson, S.N. Houde-Walter, D.T. Moore, D.P. Ryan, and J.M. Stigaman, "Design of a gradient-index photographic objective," *Appl. Opt.*, vol. 21, 993-998, 1982.
47. K.P. Thompson and L. Hoyle, "A key to cost effective optical systems," *Proc. of SPIE*, vol. 22, 1994.
48. G. J. Tearney, M. E. Brezinski and J. F. Southern, B. E. Bouma, M. R. Hee, and J. G. Fujimoto, "Determination of the refractive index of highly scattering human tissue by optical coherence tomography," *Opt. Lett.*, vol. 20, 2258-2260, 1995.
49. A.M. Rollins, M.D. Kulkarni, S. Yazdanfar, R. Ung-arunyawee, and J.A. Izatt, "In vivo video rate optical coherence tomography," *Opt Exp.*, vol. 3, 219-229, 1998